

Syngas production via the biogas dry reforming reaction over nickel supported on modified with CeO₂ and/or La₂O₃ alumina catalysts



N.D. Charisiou ^a, G. Siakavelas ^a, K.N. Papageridis ^a, A. Baklavaridis ^a, L. Tzounis ^b, D.G. Avraam ^{a,c}, M.A. Goula ^{a,*}

^a Laboratory of Alternative Fuels and Environmental Catalysis (LAFEC), Department of Environmental and Pollution Control Engineering, School of Technological Applications, Technological Education Institution of Western Macedonia, GR – 50100, Koila, Kozani, Greece

^b Laboratory for Thin Films-Nanosystems and Nanometrology (LTFN), Department of Physics, Aristotle University of Thessaloniki, GR – 54124, Thessaloniki, Greece

^c Department of Environment and Hydroeconomy, Regional Unity of Imathia, Region of Central Macedonia, GR – 59131, Veria, Greece

ARTICLE INFO

Article history:

Received 30 July 2015

Received in revised form

27 January 2016

Accepted 13 February 2016

Available online 26 February 2016

Keywords:

Biogas valorization

Syngas production

Ni catalysts

Ceria modified alumina

Lanthana modified alumina

Dry reforming

ABSTRACT

In this study, an investigation of the effects of the modification of aluminum oxide (Al_2O_3) with various dopants, namely CeO_2 and/or La_2O_3 for Ni based catalysts (Ni/CeAl , Ni/LaAl and Ni/CeLaAl) synthesized via the wet impregnation method at a constant nickel loading (8 wt. %), was performed for the biogas dry reforming reaction. The final catalysts, at their calcined or/and reduced form, were characterized by various techniques, such as XRD, SEM, and N_2 adsorption–desorption isotherms. The chemical composition of the catalysts was determined by ICP. Used catalysts were characterized by SEM and RAMAN, in order to establish whether carbon was deposited and its nature. A theoretical model has also been developed, with the aim of assessing the experimental behavior of the fixed bed reactor and the catalysts tested herein. Catalytic performance of all catalysts concerning the biogas dry reforming reaction was studied in order to investigate the effect of the reaction temperature on methane (X_{CH_4}) and carbon dioxide (X_{CO_2}) conversion, hydrogen (Y_{H_2}) and carbon monoxide (Y_{CO}) yield, and H_2/CO molar ratio of the produced gas mixture at the outlet of the reactor. The results indicate that modification of Ni/Al catalysts with CeO_2 and/or La_2O_3 significantly enhances catalytic performance, with catalysts containing lanthanum (i.e., Ni/LaAl and Ni/CeLaAl) performing better than the sample containing only ceria (Ni/CeAl).

© 2016 Elsevier B.V. All rights reserved.

1. Introduction

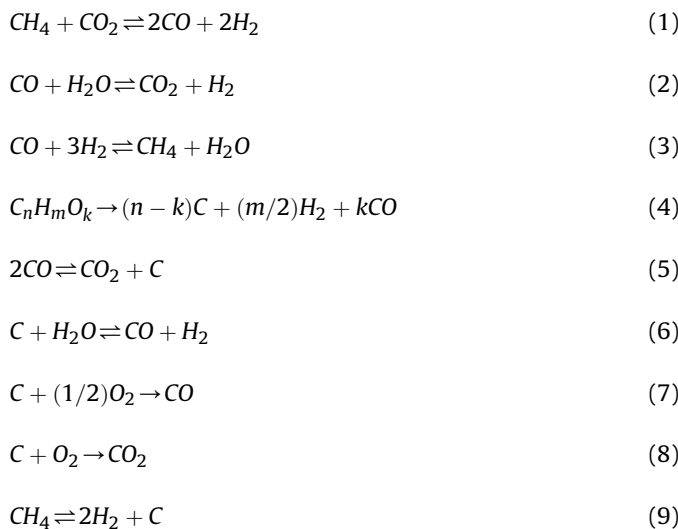
As is well documented, the unprecedented development that the world has experienced since the 1950's has been based upon an ever increasing demand for energy. Although the benefits are obvious, the environmental problems emanating from the use of fossil fuels are of such grave importance that they are increasingly moving towards the top of the international political and economic agenda (Mathews, 2014; Charisiou and Goula, 2014). Prominent amongst these are the results that anthropogenic Green House Gas (GHGs) emissions have on the planet's climate. The finite nature of fossil resources are also a cause of anxiety, as is the insecurity surrounding the reliability of future energy supplies (Almeida and

Silva, 2009; Ang et al., 2015). Among the various Renewable Energy Systems (RES) that are being developed, the utilization of biogas presents an attractive option as it is obtained mainly by the anaerobic digestion of biomass coming from different sources such as sewage, sludge, landfill or industry. The major constituents of the biogas are CO_2 and CH_4 , thus it could be processed to synthesis gas by reforming reactions (Goula et al., 2014, 2015).

The Dry Reforming of Methane (DRM, (Eq. (1))) is a highly endothermic catalytic reaction that produces a syngas with a theoretical $\text{H}_2:\text{CO}$ molar ratio of 1:1. Side reactions like Water Gas Shift (WGS, (Eq. (2))), methanation (Eq. (3))), carbon formation (Eq. (4)), carbon monoxide disproportionation (Boudouard reaction, (Eq. (5))), gasification reaction (Eq. (6)), oxidation reactions (Eqs. (7) and (8)) and methane decomposition (Eq. (9)) can take place on the catalyst surface, affecting the performance of the above mentioned processes.

* Corresponding author.

E-mail address: mgoula@teiwm.gr (M.A. Goula).



During the last years, the DRM has been intensively investigated for the production of synthesis gas (Odedairo et al., 2013; Djinović et al., 2012; Xiangyu et al., 2012; Ni et al., 2012; Lemonidou et al., 1998). One of the primary limitations of the dry reforming technology is catalyst deactivation; this occurs due to carbon deposition during the high temperature process (Goula et al., 1996; Serrano-Lotina and Daza, 2014). Therefore, the development of a catalyst resistant to carbon deposition during CO₂ reforming of CH₄ is one of the main issues of this technology. Recent research efforts have focused on developing catalysts that minimize the rate of methane decomposition and/or CO disproportion (Koo et al., 2014; Angeli et al., 2013; Liu et al., 2011; Plou et al., 2014).

Nickel (Ni) based catalysts have attracted interest because they have lower cost and higher availability than noble metal catalysts, and a considerable intrinsic activity, especially when the Ni is highly dispersed over the support (Sajjadi et al., 2013; Rahemi et al., 2013; Aghamohammadi et al., 2013). However, as already mentioned, they suffer from deactivation due to carbon formation (with carbon tending to deposit and cover the active sites of the catalyst's surface), and metal particles sinterization, due to a lack of adequate thermal stability (Therdthianwong et al., 2008; Pompeo et al., 2007). Alumina-based supports have been investigated mainly due to alumina's high specific area which improves metal dispersion (Bereketidou and Goula, 2012). Nevertheless, the use of alumina as support promotes catalysts deactivation by deposition of carbon and catalyst sintering. The formation of coke deposits has been associated with dehydration, cracking and polymerization reactions, which take place on the acid sites of alumina, while sintering has been associated with a transition of alumina to crystalline phase during reaction (Bereketidou and Goula, 2012). Several strategies have been developed in an effort to minimize carbon deposition upon Ni catalytic surface during reforming reactions; one of the first was the SPARG (sulfur – passivated reforming) process developed by Rostrup-Nielsen (1995). According to this process (Dibbern et al., 1986), the industrial steam reformer operation at conditions that would otherwise have resulted to carbon deposition could be allowed, with the utilization of the sulfur passivation of the nickel catalysts. The idea behind the SPARG process was the preferential adsorption of sulfur to the catalytically active sites, in order for the carbon nucleation to be inhibited (Rostrup-Nielsen, 1984). It was applied for CO-rich syngas production, (Udengaard et al., 1992) while the CO₂ reforming was further explored (Rostrup-Nielsen and Hansen, 1993) for noble metal catalysts.

Other efforts that aim to overcome the problems mentioned

above, focus on the use of basic additives or promoters such as CeO₂, SiO₂, La₂O₃, BaO, CaO, SrO, MgO and ZrO₂, especially on alumina, for the development of more stable supports (Bereketidou and Goula, 2012; de Sousa et al., 2012).

The well known oxygen capacity of the cerium oxide can be attributed to its oxygen deficiency in reducing environments (CeO_{2-x}) that causes its gradual oxidation to CeO₂ in oxidizing environments (Trovarelli, 1996). Thus, it can be expected that the modification of catalysts supported on alumina with ceria will result in significant improvements in their performance (Taylor, 1993; Lu et al., 2008; Xue et al., 2009). As a matter of fact, it has been proven that Ni on ceria or ceria–alumina based catalysts that have been tested for the DRM reaction exhibit improved resistance to carbon deposition and higher active phase dispersion (Wang and Lu, 1998). Additionally, it has been proven that the presence of CeO₂ stabilizes the alumina structure at high temperatures and prevents its transformation into low-surface area phases (Morterra et al., 1996). Recently, Chen et al., have reported that the formation of CeAlO₃ phase significantly enhances the catalyst carbon-resistance without decreasing the DRM activity, while it shows ability for decomposing CO₂ to form active surface oxygen and therefore the carbon-resistance promotion by nature is suggested to be contributed to an oxidative environment around Ni particles (Chen et al., 2013a).

On the other side, the basic character of lanthanum oxide (La₂O₃) resulted in promotional effects in the cases that it has been used as support or as alumina modifier for the traditional DRM nickel catalysts, as it favors CO₂ adsorption and dissociation contributing to deposited carbon gasification and thus, prevention of deactivation (Zhang et al., 1996; Slagtern et al., 1997; Verykios, 2003). It has also been proven (Martinez et al., 2004) that an increase in Ni dispersion in samples containing La leads to more metallic particles with diameters less than 10 nm that contribute to the catalytic conversion without producing large amounts of coke in filaments (Martínez et al., 2004). Liu et al., reported that the improved performance of nickel supported on lanthana–alumina catalysts with a La/Al ratio equals to 0.05 resulted at highly dispersed La species on the catalytic surface (Liu et al., 2003). A catalytic tri-reforming process applied to simulated biogas with Ni/LaCeO mixed oxides revealed that the highest catalytic activity was obtained with the Ce_{0.70}La_{0.20}Ni_{0.10}O_{2-δ} sample most probably related with the interactions of nickel–lanthana–surface oxygen vacancies of ceria that enhances the nickel dispersion (Pino et al., 2014).

In this contribution, a comparative study of catalytic performance for nickel supported on un-promoted and promoted with CeO₂, La₂O₃ and CeO₂–La₂O₃ alumina catalysts for the biogas dry reforming reaction is reported. Catalysts were synthesized applying the wet impregnation method at a constant metal loading (8 wt.%), in order to investigate the effect of the reaction temperature on the (i) methane and carbon dioxide conversion, (ii) hydrogen and carbon monoxide yield, and (iii) H₂/CO molar ratio of the produced gas mixtures at the outlet of the reactor.

The synthesized samples at their calcined and/or reduced form were characterized by various techniques such as X-Ray Diffraction (XRD), Scanning Electron Microscope (SEM) and N₂ adsorption/desorption isotherms. Their chemical composition was determined using the Inductively Coupled Plasma Emission Spectrometry (ICP). Used catalysts were characterized by SEM and RAMAN, in order to establish whether carbon was deposited and its nature.

Catalytic testing experiments were performed in a fixed-bed reactor at temperatures ranging from 500 to 800 °C and a feed gas mixture with a molar CH₄/CO₂ ratio of 1.5, simulating an ideal model biogas. Stability tests were conducted at 750 °C for a period of 20 h.

In addition a theoretical model has been developed to describe the catalytic process. The tubular experimental reactor was modeled as a heterogeneous fixed bed reactor taking explicitly into account axial mass and heat dispersion and external (inter-particle) mass and heat transport phenomena, whilst radial dispersion and internal mass and heat transport phenomena were neglected and the latter were replaced by effectiveness factors.

2. Materials and methods

2.1. Catalyst preparation

The alumina support was purchased in pellet form from Akzo Nobel N.V. (Specific Surface Area, SSA = 281 m² g⁻¹), while the lanthanum–alumina (containing 4 wt. % La₂O₃, SSA = 176 m² g⁻¹) was obtained from W.R. Grace (MI-386) in powder form. The γ-Al₂O₃ support was crushed and sieved to 350–500 μm, while the LaAl support was first pelletized and then crushed and sieved to the same size. The as prepared supports were calcined at 800 °C for 4 h, in ambient air in a static environment.

The ceria–alumina and the ceria–lanthanum–alumina supports were obtained by impregnating the alumina and the lanthanum–alumina supports with an aqueous solution of Ce(NO₃)₃·6H₂O (Sigma Aldrich Co. LLC) with appropriate ceria concentration (so as the ceria's content would be 10%). These were air dried at 120 °C for 12 h before being calcined, with the procedure described above, at 800 °C for 4 h.

The catalysts were prepared via the wet impregnation technique using Ni(NO₃)₂·6H₂O aqueous solutions with the proper concentration, in order to obtain final catalysts with Ni content of about 8 wt. %. The nickel nitrate for the catalyst preparation was obtained from Sigma Aldrich Co. LLC.

All slurries were evaporated using a rotary evaporator at 75 °C for 5 h and dried at 120 °C for 12 h followed by calcination at 800 °C for 4 h. The samples were labeled as Ni/Al, Ni/LaAl, Ni/CeAl and Ni/CeLaAl.

2.2. Catalyst characterization

The Specific Surface Area (SSA) of the catalytic samples were determined by the N₂ adsorption–desorption isotherms at –196 °C using the Nova 2200e (Quantachrome Instruments) flow apparatus, according to Brunauer–Emmett–Teller (BET) equation at the relative pressure in the range of 0.05–0.30. SSA was measured on the calcined samples.

The total pore Volume (V_p) calculation was based on nitrogen volume at the highest relative pressure, whereas the average pore size diameter was determined by the Barrett–Joyner–Halenda (BJH) method. Prior to the measurements the samples were degassed at 350 °C for 5 h under vacuum. V_p was measured on the calcined samples.

The total metal loading (wt. %) of the final catalysts was determined by Inductively Coupled Plasma Atomic Emission Spectroscopy (ICP-AES) on a Perkin–Elmer Optima 4300DV apparatus. The methodology used has been described previously (Goula et al., 2015). Here, it will suffice to state that the wavelengths selected were at 341.476, 227.022, and 231.604 nm, and that the selected conditions of the measurement were: Plasma flow: 15 L/min, Auxiliary flow: 0.2 L/min, Nebulize flow: 0.6 L/min, RF Power: 1300 W, Plasma View: radial view, and Sample Flow Rate: 2 mL/min. ICP was measured on the calcined samples.

The catalysts crystalline structure was determined by applying the X-ray diffraction (XRD) technique, using a ThermoAl diffractometer at 40 kV and 30 mA with Cu Kα radiation ($\lambda = 0.154178$ nm). Diffractograms were recorded in the $2\theta = 2\text{--}70^\circ$

range at a scanning rate of 0.04° over 1.2 min⁻¹. The diffraction pattern was identified by comparison with those of known structure in the International Centre for Diffraction Data database. The XRD technique was used for both calcined and reduced samples. The Scherrer equation (Eq. (10)) was employed to determine the particle size of different phases based on their most intense diffraction peaks.

$$L = \frac{2^{1/2} \times \lambda}{\beta \times \cos \theta} \quad (10)$$

where L is the average width of the crystallite (nm), λ is the wavelength of incident radiation (nm), β is the half-height width of the most intense peak for the species (radians), and θ is half the Bragg angle of that peak (°). Morphological examination of both fresh and used catalysts was done using Scanning Electron Microscopy (SEM) in a JEOL 6610LV (SEAL LABORATORIES). The elemental analysis, by means of Energy Dispersive Spectroscopy (EDS), was carried out using a large area (80 mm²) silicon drift detector (Oxford Instruments X-Max 80). Images, elements maps and spectra were acquired and analyzed with the AZtech Nanoanalysis software (Oxford Instruments).

The coke deposited on spent catalyst samples was characterized by Raman spectroscopy under atmospheric conditions without pre-treatment using a WITEC GmbH alpha300R micro-Raman system. The illumination and collecting optics of the system consist of an Optical Microscope in confocal configuration. The system achieves the high contrast required for the rejection of the elastically scattered component by an edge filter. The backscattered light is dispersed by a 1800 line/mm grating and the Raman signal is detected by a Peltier Cooled CCD detector (203 K, 1024 × 256 pixel CCD detector). The spectra were acquired with a 20× long distance objective with an excitation wavelength of 532 nm from an Ar⁺ ion laser with a laser power set at 2 mW (calibrated against a silicon standard). Nominal spectral resolution was about 1 cm⁻¹ and all spectra were collected with 3 accumulations per spectrum, 5 s spectra acquisition time in the spectral range of 600–3300 cm⁻¹. For each sample, at least three Raman spectra were collected in different areas to assess the homogeneity of the investigated material. All the spectra collected from the same sample showed the same features confirming the homogeneity of the carbon deposits.

2.3. Catalytic tests

The experimental procedure has been analyzed in detail previously (Goula et al., 2015). Briefly, a fixed bed reactor was used for the catalytic performance testing experiments, within the temperature range of 500–800 °C, at atmospheric pressure (Fig. 1). The total flow rate used was 100 ml/min, consisting of a gas mixture of CH₄/CO₂/He (30 v/v%, 20 v/v% and 50 v/v% respectively), corresponding to a Weight Hourly Space Velocity (WHSV) of 120,000 ml g⁻¹ h⁻¹. Thus, a diluted simulating biogas mixture, with a CH₄ to CO₂ molar ratio equal to 1.5, was used as feed in the reactor inlet (Bereketidou and Goula, 2012).

The gaseous reaction products were analyzed on-line by gas chromatography in an Agilent GC-systems-7890A gas chromatographer with two columns in parallel, Agilent J&W HP-PLOT Q (19095-Q04, 30 m length, 0.530 mm I.D.) and Agilent J&W HP-PLOT Molesieve (19095P-MSO, 30 m length, 0.530 mm I.D.), equipped with TCD and FID detectors (the GC carrier gas was He 5.5). Prior to performing any catalytic reaction measurement, catalysts were in situ activated (reduced) by flowing pure hydrogen for 2 h at 800 °C. Following activation, the temperature was reduced to 500 °C, under a flow of He 5.0 (100 ml/min for 1 h). Then the reaction mixture was fed into the reactor and the temperature was increased stepwise,

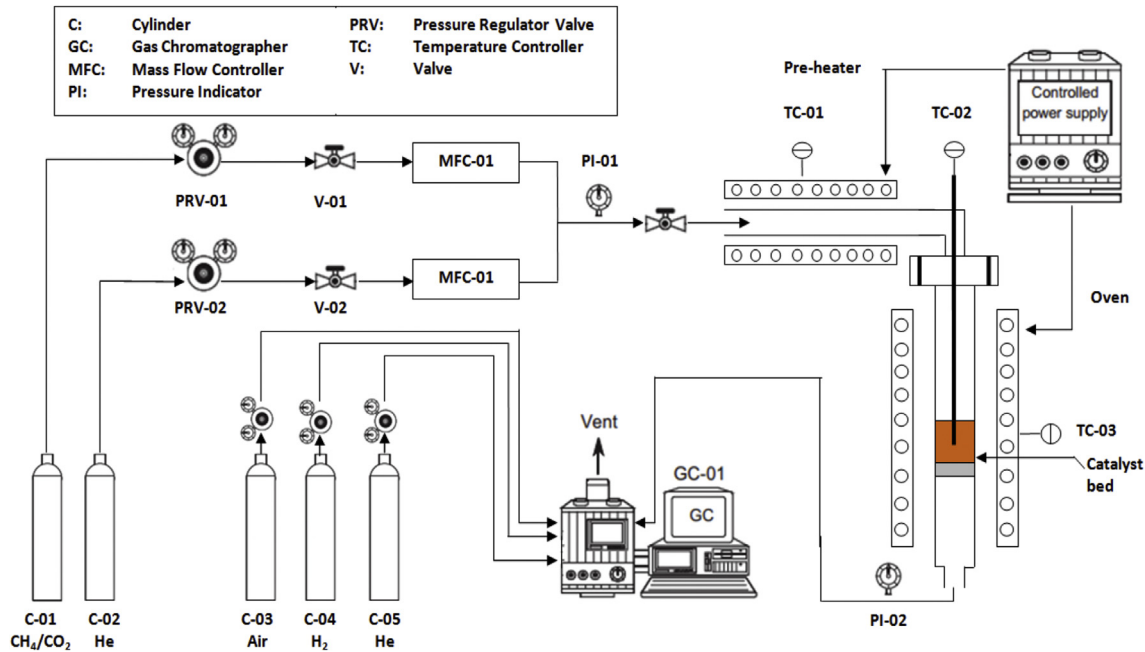


Fig. 1. Schematic flow chart of experimental setup for activity test of catalysts towards biogas dry reforming.

remaining for 45 min at each step in order to ensure operation at steady state conditions. For the time on stream experiments, the same procedure described above was followed, only this time the temperature after activation was reduced at 750 °C and measurements were taken at hourly intervals.

The values of (i) methane (CH_4) conversion, (ii) carbon dioxide (CO_2) conversion, (iii) hydrogen (H_2) yield, (iv) carbon monoxide (CO) yield, and (v) H_2/Co molar ratio were determined according to the following equations:

$$X_{\text{CH}_4} (\%) = \frac{F_{\text{CH}_4,\text{in}} - F_{\text{CH}_4,\text{out}}}{F_{\text{CH}_4,\text{in}}} \times 100 \quad (11)$$

$$X_{\text{CO}_2} (\%) = \frac{F_{\text{CO}_2,\text{in}} - F_{\text{CO}_2,\text{out}}}{F_{\text{CO}_2,\text{in}}} \times 100 \quad (12)$$

$$Y_{\text{H}_2} (\%) = \frac{F_{\text{H}_2}}{2F_{\text{CH}_4,\text{in}}} \times 100 \quad (13)$$

$$Y_{\text{CO}} (\%) = \frac{F_{\text{CO}}}{F_{\text{CH}_4,\text{in}} + F_{\text{CO}_2,\text{in}}} \times 100 \quad (14)$$

$$\text{Molar ratio} = \frac{F_{\text{H}_2,\text{out}}}{F_{\text{CO},\text{out}}} \quad (15)$$

where $F_{i,\text{in}}$ or $F_{i,\text{out}}$ is the flow rate of each component in feed or effluent.

3. Theoretical investigation

3.1. Reactor modeling

A 1-D heterogeneous model was developed to describe the steady-state behavior of the steam reforming tubular fixed bed reactor, based on the following assumptions:

- (a) Plug-flow conditions;
- (b) Significant axial mass and heat dispersion with negligible radial gradients;
- (c) Resistances to external mass and heat transport were taken explicitly into account;
- (d) Resistances to internal mass and heat transport were replaced by effectiveness factors;
- (e) Uniform particle size;
- (f) Constant bed porosity;
- (g) Only heterogeneous gas phase reactions were considered;
- (h) Five reactive species (CH_4 , CO_2 , H_2O , CO , H_2) plus an inert gas (He) were included in the model.

The model was developed in a flexible way, so that adiabatic conditions instead of isothermal conditions could be incorporated in it and axial temperature distribution could be taken into account. The same holds for cooling conditions, where an external cooling fluid of variable temperature could be incorporated in the calculations of the reactor temperature axial distribution.

The main equations of the model (mass, momentum and energy balances) are presented below:

3.1.1. Mass balances Species molar fluxes

$$\frac{1}{L} \frac{\partial N_i}{\partial z} = -k_{m,i} a_v (c_i - c_i^s) \quad (16)$$

Total molar flux

$$N = \sum_{i=1}^{N_c} N_i \quad (17)$$

Species bulk concentrations

$$N_i = v c_i - \frac{1}{L} \epsilon D_z c \frac{\partial x_i}{\partial z} \quad (18)$$

Total bulk concentration

$$c = \frac{\rho}{M}$$

Species surface concentrations

$$k_{m,i} a_v (c_i - c_i^s) = -\rho_B \sum_{j=1}^{N_R} \eta_j \nu_{ij} R_j \quad (20)$$

Total surface concentration

$$c^s = \sum_{i=1}^{N_c} c_i^s \quad (21)$$

Superficial velocity

$$N = vC$$

3.1.2. Momentum balance

$$\frac{1}{L} \frac{\partial P}{\partial z} = \frac{1}{L} v^2 \frac{\partial \rho}{\partial z} - \frac{\rho v^2}{d_p} \frac{(1-\varepsilon)}{\varepsilon^3} \left(150 \frac{1-\varepsilon}{Re} + 1.75 \right) \quad (23)$$

3.1.3. Energy balance

Bulk temperature

$$E = \rho v \hat{H}(x_i, T, P) - \frac{1}{L} k_z \frac{\partial T}{\partial z} \quad (24)$$

Energy flux

$$E = \rho v \hat{H}(x_i, T, P) \quad (\text{isothermal reactor}) \quad (25a)$$

$$\frac{1}{L} \frac{\partial E}{\partial z} = -h_g a_v (T - T^s) \quad (\text{adiabatic reactor}) \quad (25b)$$

$$\frac{1}{L} \frac{\partial E}{\partial z} = -h_g a_v (T - T^s) - \frac{4U_{tc}}{d_t} (T - T_{cool}) \quad (\text{cooled reactor}) \quad (25c)$$

Solid temperature

$$h_g a_v (T - T^s) = -\rho_B \sum_{j=1}^{N_R} \eta_j (-\Delta H_{Rj}) R_j = \rho_B \sum_{i=1}^{N_c} \bar{H}_i r_i \quad (26)$$

To reach a closure for this problem, gas mixture density, molecular weight, heat capacity and enthalpy should be calculated with the help of a suitable physicochemical properties model according to:

Density

$$\rho = \rho(x_i, T, P) \quad (27)$$

Mean molecular weight

$$M = M(x_i, T, P) \quad (28)$$

Heat capacity

$$C_{pg} = C_{pg}(x_i, T, P) \quad (29)$$

Enthalpy

$$\hat{H} = \sum_{i=1}^{N_c} x_i \left(\hat{H}_{f,i}^0 + \int_{T_{ref}}^T c_{pi} dT \right) + \hat{H}^R \quad (30)$$

Finally, mass and heat transport properties were obtained from empirical correlations suitable for experimental scale reactors, as functions of local values of dimensionless Reynolds, Prandtl and Schmidt numbers according to:

$$D_z, k_z, k_{m,i}, h_g = f(\text{Re}, \text{Pr}, \text{Sc}_i) \quad (31)$$

All pertinent variables and parameters of the problem are as presented below:

N_i is the molar flux of species i [mol/m² s], $i = 1, \dots, N_c$,
 N_c is the number of reactive species,
 N is the total flux of the gas mixture [mol/m² s],
 c_i is the bulk concentration of species i [mol/m³],
 x_i is the molar fraction of species i ,
 c is the total bulk concentration [mol/m³],
 c_i^s is the surface concentration of species i [mol/m³],
 c^s is the total surface concentration [mol/m³],
 R_j is the rate of the reaction j [mol/kg cat s], $j = 1, \dots, N_R$,
 N_R is the number of reactions,
 $-\Delta H_{Rj}$ is the heat of the reaction j [J/mol],
 r_i is the rate of production or consumption of species i [mol/kg cat s],
 \hat{H}_i is the partial molar enthalpy of species i [J/mol],
 ν_{ij} is the stoichiometric coefficient of species i in the j th reaction,
 η_j is the effectiveness factor of the j th reaction,
 T is the local temperature of the bed [K],
 T^s is the local particle temperature [K],
 T_{cool} is the local temperature of the cooling fluid [K],
 P is the pressure along the bed [Pa],
 E is the mixture energy flux [J/m² s],
 \hat{H} is the mixture mass enthalpy [J/Kg],
 $\hat{H}_{f,i}^0$ is the formation enthalpy of the species i [J/Kg],
 \hat{H}^R is the mixture residual mass enthalpy [J/Kg],
 c_{pi} is the mass heat capacity of species i [J/Kg K],
 ϵ is the (constant) porosity of the bed,
 ρ_B is the bulk density of the bed [kg/m³],
 ρ is the density of the gas mixture [kg/m³],
 M is the gas mixture molecular weight [Kg/mole],
 v is the superficial (Darcy's) velocity of the gas mixture [m/s],
 d_p is the (uniform) equivalent particle diameter [m],
 α_v is the specific area of the catalytic particle [1/m],
 μ is the gas mixture viscosity [Pa s],
 C_{pg} is the mixture mass heat capacity [J/Kg K],
 k_g is the mixture thermal conductivity [J/m s K],
 $D_{eff,i}$ is the effective diffusivity of species i [m²/s],
 D_z is the axial mass dispersion coefficient [m²/s],
 k_z is the effective thermal conductivity [J/m s]
 $k_{m,i}$ is the film mass transfer coefficient of species i [m/s],
 h_g is the film heat transfer coefficient [J/m² s K],
 U_{tc} is the overall heat transfer coefficient [J/m² s K],
 $\text{Re} = \frac{\rho v d_p}{\mu}$ is the Reynolds number,
 $\text{Pr} = \frac{C_{pg}\mu}{k_g}$ is the Prandtl number,
 $\text{Sc}_i = \frac{\mu}{\rho D_{eff,i}}$ is the Schmidt number of species i ,
 L is the length of the reactor [m],
 d_t is the reactor tube diameter [m],
 $z = \frac{x}{L}$ is the (dimensionless) bed length coordinate.

Additionally, four more equations were introduced in the system of equations, namely the equations for the conversion of methane and carbon dioxide and the equations for hydrogen and carbon monoxide yield, Eqs. (11) and (12) and Eqs. (13) and (14), respectively, where flow rates were replaced by the corresponding molar fluxes.

Equations (11)–(14), (16)–(31) form a system of $3N_C+13$ coupled ordinary differential and algebraic equations (DAE system) for $3N_C+13$ primary dependent variables. The model was implemented and solved in ATHENA Visual Studio process modeling environment (Athena Visual Software, Inc.). The problem is augmented with the appropriate initial values given by:

At the reactor inlet, $z = 0$:

$$T = T_{in}, \quad P = P_{in}, \quad v = v_{in},$$

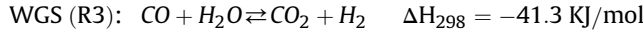
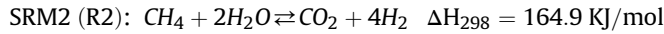
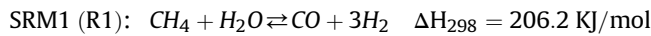
$$\rho = \rho(x_{i,in}, P_{in}, T_{in}), \quad c = \frac{\rho(x_{i,in}, P_{in}, T_{in})}{M(x_{i,in}, P_{in}, T_{in})}, \quad N = v_{in}c_{in},$$

$$N_i = v_{in}c_{in}x_{i,in}, \quad v_{in}c_{in}x_{i,in} = v_c - \frac{1}{L}\epsilon D_z c \frac{\partial x_i}{\partial z}, \quad k_{m,i}a_v(c_i - c_i^s) \\ = -\rho_B \sum_{j=1}^{N_R} \eta_j v_{ij} R_j,$$

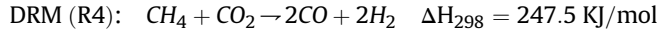
$$E = \rho v \hat{H}(x_{i,in}, P_{in}, T_{in}), \quad h_g a_v(T - T^s) \\ = -\rho_B \sum_{ij=1}^{N_R} \eta_j (-\Delta H_{Rj}) R_j = \rho_B \sum_{i=1}^{N_C} \bar{H}_i r_i \quad (32)$$

3.2. Reaction kinetics model for dry reforming of methane

Among the many possible reactions that can occur during methane dry reforming and form the prevailing reaction scheme, as reported in the literature (Jun et al., 2011) and in the Introduction of the present study [Eqs. (1)–(9)], a limited number of them is included in theoretical models in order to keep them tractable. The following reactions were included in the present study:



in addition to the prevailing reaction of dry reforming:



Except for the WGS reaction the rest of the reactions above are endothermic, therefore the overall process is endothermic and a certain amount of heat is needed to maintain methane conversion. However, the amount of the heat consumed in the overall reaction depends on the relative rates of reaction attainable by each one of the prevailing reactions according to the catalytic system and the experimental conditions. Generally, considerable amounts of heat should be supplied to the reactor in order to maintain the desired high temperature.

Heat of reactions as well as reaction rates for the scheme presented above are well established in the literature, whereas specific adjustments should be done to make them usable in different catalytic systems. The model described by Xu and Froment (Xu and Froment, 1989) for the steam reforming reactions has been

extensively tested at laboratory scale over different Ni-based catalysts, doped with suitable dopants, as the Ce and La used in the present study.

The reaction rate equations for the first three prevailing reactions that were taken into consideration in the present study are given below:

$$R_1 = \frac{k_{SRM1} \left(P_{\text{CH}_4} P_{\text{H}_2\text{O}} - P_{\text{H}_2}^3 P_{\text{CO}} / K_{pSRM1} \right) / P_{\text{H}_2}^{2.5}}{\left[1 + K_{\text{CO}} P_{\text{CO}} + K_{\text{H}_2} P_{\text{H}_2} + K_{\text{CH}_4} P_{\text{CH}_4} + K_{\text{H}_2\text{O}} (P_{\text{H}_2\text{O}} / P_{\text{H}_2}) \right]^2} \quad (33)$$

$$R_2 = \frac{k_{SRM2} \left(P_{\text{CH}_4} P_{\text{H}_2\text{O}}^2 - P_{\text{H}_2}^4 P_{\text{CO}_2} / K_{pSRM2} \right) / P_{\text{H}_2}^{3.5}}{\left[1 + K_{\text{CO}} P_{\text{CO}} + K_{\text{H}_2} P_{\text{H}_2} + K_{\text{CH}_4} P_{\text{CH}_4} + K_{\text{H}_2\text{O}} (P_{\text{H}_2\text{O}} / P_{\text{H}_2}) \right]^2} \quad (34)$$

$$R_3 = \frac{k_{WGS} (P_{\text{CO}} P_{\text{H}_2\text{O}} - P_{\text{H}_2} P_{\text{CO}_2} / K_{pWGS}) / P_{\text{H}_2}}{\left[1 + K_{\text{CO}} P_{\text{CO}} + K_{\text{H}_2} P_{\text{H}_2} + K_{\text{CH}_4} P_{\text{CH}_4} + K_{\text{H}_2\text{O}} (P_{\text{H}_2\text{O}} / P_{\text{H}_2}) \right]^2} \quad (35)$$

As for the dry reforming overall reaction (DRM), a Langmuir–Hinshelwood type reaction is usually reported (Rostrup-Nielsen and Hansen, 1993; Olsbye et al., 1997; Osaki et al., 1994), and the reaction rate is expressed on the basis of the assumption that the surface reaction is the rate determining step, according to:

$$R_4 = \frac{k_{DRM} \left(P_{\text{CH}_4} P_{\text{CO}_2} - P_{\text{H}_2}^2 P_{\text{CO}}^2 / K_{pDRM} \right)}{(1 + K_1 P_{\text{CH}_4} + K_2 P_{\text{CO}})(1 + K_3 P_{\text{CO}_2})} \quad (36)$$

Utilization of carbon dioxide in methane reforming can lead to carbon deposition and subsequently to catalyst deactivation. However, catalyst stability test performed in the present study revealed that stable activity of the catalysts could be maintained for over 20 h for the Ni/CeLaAl, Ni/LaAl and Ni/CeAl catalysts, under appropriate experimental conditions and only for the Ni/Al the time of stable operation is limited to the first 5 h. Therefore, the assumption that carbon deposition is negligible is adopted here in order to develop a theoretical model to describe the steady-state operation of the experimental reactor, at least during the initial stages of methane dry reforming.

However, application of this model on four different catalytic systems requires some additional adjustment. For the case of the Ni based on Al_2O_3 catalysts studied in the present work, adjustment concerning the activity of the catalyst was required. This was done carefully, because the catalysts activity may be influenced by heat and mass transport resistances as well. To this end, adjustments were imposed on the effectiveness factors that represent the internal heat and mass transport limitations, and on the dry reforming reaction kinetics parameters, i.e. Arrhenius pre-exponential factor and activation energy of the DRM reaction. Therefore, effectiveness factors, η_j , were used to account for intraparticle transport limitations for all reactions taken into consideration in the model and DRM kinetics parameters to account for the altered activity of the doped catalysts.

The Arrhenius kinetics parameters and the activation energies are given in Table 1. Van't Hoff parameters for species adsorption for steam reforming, water gas shift and dry reforming are given in Table 2. Specific values of the kinetics parameters were taken from (Koh et al., 2007), whereas those pertinent to DRM reaction rates were used as initial values for subsequent estimation of their values. According to this reference, reaction equilibrium constants

Table 1

Kinetic reaction data.

Reaction	$\ln k_{j,b}^a$	E_j/RT_b^b
1	6.032	25.433
2	4.052	28.492
3	2.674	8.716
4	6.653 ^c	24.160 ^d

^a $k_{j,b}$ [=] mol/kg_{cat}.s.bar^{-0.5} (1, 2) bar (3) bar² (4).^b E_j [=] J/mol.^c Initial value for the estimation procedure.^d Initial value for the estimation procedure.**Table 2**

Van't Hoff parameters for species adsorption.

Species	K_{oi} (bar ⁻¹)	ΔH_i (J/mol)
CH ₄	$6.65 \cdot 10^{-4}$	-38,280
H ₂ O	$1.77 \cdot 10^5$	88,680
CO	$8.23 \cdot 10^{-5}$	-70,650
H ₂	$6.12 \cdot 10^{-9}$	-82,900

$$K_1 = 0.50 \text{ bar}^{-1}, K_2 = 9.71 \text{ bar}^{-1}, K_3 = 26.1 \text{ bar}^{-1}$$

are given by:

$$K_{pSRM1} = e^{\left(-\frac{26.200}{T_b} + 29.71 \right)} \text{ bar}^2 \quad (37)$$

$$K_{pSRM2} = e^{\left(-\frac{23.400}{T_b} + 27.40 \right)} \text{ bar}^2 \quad (38)$$

$$K_{pWGS} = K_{pSRM2}/K_{pSRM1} \quad (39)$$

$$K_{pDRM} = K_{pSRM1}/K_{pWGS} \text{ bar}^2 \quad (40)$$

In order to reduce the temperature dependency and to facilitate the parameter estimation procedure, the temperature dependence of Arrhenius kinetics parameters is expressed as:

$$k_j(T) = k_j(T_b)e^{\left[\frac{E_{aj}}{RT_b} \left(1 - \frac{T_b}{T} \right) \right]} = k_{j,b}e^{\left[E_{j,b} \left(1 - \frac{T_b}{T} \right) \right]} \quad (41)$$

where, T_b is a base temperature, namely 850 °C in the present study.

Van't Hoff species adsorption parameters are expressed as:

$$K_i = K_{oi} e^{\left(-\frac{\Delta H_i}{RT} \right)} \quad (42)$$

whereas, constant values apply to the DRM adsorption parameters.

By summing up the reaction rates, R_j , of all reactions j to which a species i is participating, the rate of production or consumption of that species is determined. For the present reaction scheme, taking also into account the corresponding stoichiometric coefficients, the reaction rates are expressed respectively by:

$$r_{CH_4} \equiv r_1 = -\eta_1 R_1 - \eta_2 R_2 - \eta_4 R_4 \quad (43)$$

$$r_{CO_2} \equiv r_2 = \eta_2 R_2 + \eta_3 R_3 - \eta_4 R_4 \quad (44)$$

$$r_{H_2O} \equiv r_3 = -\eta_1 R_1 - 2\eta_2 R_2 - \eta_3 R_3 \quad (45)$$

$$r_{CO} \equiv r_4 = \eta_1 R_1 - \eta_3 R_3 + 2\eta_4 R_4 \quad (46)$$

$$r_{H_2} \equiv r_5 = 3\eta_1 R_1 + 4\eta_2 R_2 + \eta_3 R_3 + 2\eta_4 R_4 \quad (47)$$

$$r_{He} \equiv r_6 = 0 \quad (48)$$

In order to estimate appropriate values for the effectiveness factors given above and for the DRM kinetics parameters, an optimization procedure was developed. An estimate of the vector of unknown parameters, $\theta^T = (\eta_1, \eta_2, \eta_3, \eta_4, k_{DRM,b}, E_{DRM,b})$, was obtained by matching the theoretically obtained methane and carbon dioxide conversions and hydrogen and carbon monoxide yields to corresponding experimental values. The model responses were thus $X_{CH_4}, X_{CO_2}, Y_{CO}$ and Y_{H_2} , obtained at all experimental settings and all experiments conducted in the present study.

For the solution of the nonlinear parameter estimation problem with multiple (four) response data, the Bayesian estimator of the GREGPLUS solver of ATHENA Visual Studio software (Stewart et al., 1992) was adapted to the numerical solution of PDAPLUS solver. Details about the parameter estimation procedure are given in Appendix A.

The properties of the real gas mixture that depend on the local temperature, pressure and molar composition were continuously calculated along the bed axial coordinate using the physical properties package of the ATHENA Visual Studio. Fluid density, molecular weight, heat capacity and molar enthalpy were the output values. An average value for the gas viscosity was used, instead.

The core of the experimental reactor was a tubular reactor made of stainless steel with 9.2 mm inner diameter. All other characteristics concerning the geometry of the bed, the catalyst properties and the gas properties are summarized in Table 3.

4. Results and discussion

4.1. Characterization results

In Table 4 the physicochemical properties of all samples are presented. As can be observed, the specific surface area was reduced with the introduction of nickel and/or ceria on the supporting material, whereas the pore volume was not significantly altered. The lower surface area can be attributed to the fact that the internal surface area of the support pore system is probably progressively covered by nickel species adsorbed on alumina active sites forming a layer (Bereketidou and Goula, 2012). However, it is important to note that all catalyst samples have comparable SSA. The ICP results show that the desired metal level was achieved for all catalysts, with the exception of the Ni/CeLaAl.

Table 5 provides a summary of the crystalline phases that were detected in the different samples and Fig. 2 shows the XRD patterns of all catalysts. More specifically, Fig. 2(a) depicts the XRD patterns of the Ni/Al catalyst after calcination and after reduction. For the calcined Ni/Al sample, characteristic peaks at $2\theta = 35.2^\circ, 47.2^\circ$ and 67.6° assigned to $\gamma\text{-Al}_2\text{O}_3$ can be observed. Peaks of the spinel nickel aluminate phase (NiAl_2O_4), indicated by the intensity of diffraction lines at $2\theta = 19^\circ, 32^\circ, 37^\circ, 45^\circ, 60.2^\circ$ and 65.9° were also detected.

Table 3

Reactor characteristics and average gas and particle properties.

	Unit	Value
Catalyst load	g	0.05
Bed diameter	mm	9.2
Reactor length	mm	5.1
Equivalent particle diameter	mm	0.425
Bed porosity	—	0.4
Bulk density	Kg/m ³	570
Gas mixture viscosity	Pa.s	$0.031 \cdot 10^{-3}$

Table 4

Characterization results of the calcined samples.

Support/Catalyst ¹	SSA ($\text{m}^2 \text{ g}^{-1}$)	V_p (ml g^{-1})	Metal loading (Ni, wt.%)
Al	195	0.65	—
CeAl	167	0.58	—
LaAl	n/a	0.70	—
CeLaAl	n/a	0.60	—
Ni/Al	158	0.58	7.14
Ni/CeAl	142	0.51	7.63
Ni/LaAl	159	n/a	7.79
Ni/CeLaAl	140	n/a	6.39

Note: n/a = non available.

Table 5

Crystalline phases of all samples.

Catalyst	Crystalline phases	Nickel species particle size (nm)
Al (c)	$\gamma\text{-Al}_2\text{O}_3$	n/a
CeAl (c)	$\gamma\text{-Al}_2\text{O}_3$, CeO_2	n/a
LaAl (c)	$\gamma\text{-Al}_2\text{O}_3$	n/a
CeLaAl (c)	$\gamma\text{-Al}_2\text{O}_3$, CeO_2	n/a
Ni/Al (c)	$\gamma\text{-Al}_2\text{O}_3$, NiAl_2O_4	18.1
Ni/Al (r)	$\gamma\text{-Al}_2\text{O}_3$, NiAl_2O_4 , Ni	16.8
Ni/CeAl (c)	$\gamma\text{-Al}_2\text{O}_3$, NiAl_2O_4 , CeO_2 , NiO	n/d
Ni/CeAl (r)	$\gamma\text{-Al}_2\text{O}_3$, NiAl_2O_4 , CeO_2 , Ni	n/d
Ni/LaAl (c)	$\gamma\text{-Al}_2\text{O}_3$, NiAl_2O_4	8.9
Ni/LaAl (r)	$\gamma\text{-Al}_2\text{O}_3$, NiAl_2O_4 , Ni	7.3
Ni/CeLaAl (c)	$\gamma\text{-Al}_2\text{O}_3$, NiAl_2O_4 , CeO_2	6.7
Ni/CeLaAl (r)	$\gamma\text{-Al}_2\text{O}_3$, NiAl_2O_4 , CeO_2 , Ni	5.1

Note: c = calcined, r = reduced, n/a = non applicable, n/d = not detected.

The formation of NiAl_2O_4 is caused by the reaction of NiO and Al_2O_3 due to the high calcination temperature (Bereketidou and Goula, 2012; Dou et al., 2014). Moreover, the nickel oxide (NiO) structure was not detected (expected at $2\theta = 43.5^\circ$ and 63.1°), indicating that if these species were present, they would be quite small, since XRD can typically only detect crystalline phases that are larger than several nm. The main differences between the XRD patterns of the calcined and reduced Ni/Al catalyst, are the decreasing intensities of Al_2O_3 and NiAl_2O_4 peaks and the appearance of small peaks due to the presence of metallic nickel (Ni^0) at $2\theta = 44^\circ$ and 51.2° .

Fig. 2(b) depicts the XRD patterns of the Ni/CeAl catalyst after calcination and after reduction. NiAl_2O_4 ($2\theta = 19.3^\circ$, 37.2° , 48.9° , 59.6° , 65.5°), CeO_2 ($2\theta = 28.5^\circ$, 33° , 47.6° , 56.4°), and Al_2O_3 ($2\theta = 26.7^\circ$, 46.4° , 66.9°) peaks appear at both the calcined and reduced sample. The main differences between the XRD patterns of the calcined and reduced Ni/CeAl catalyst, are the peaks of NiO ($2\theta = 37.5^\circ$, 43.2°) that were identified on the calcined sample and Ni^0 ($2\theta = 43.5^\circ$, 50.8°) identified on the reduced catalyst.

Fig. 2(c) depicts the XRD patterns of the Ni/LaAl catalyst after calcination and after reduction. The patterns are not too dissimilar to those presented above, as again, peaks assigned to $\gamma\text{-Al}_2\text{O}_3$ ($2\theta = 35.1^\circ$, 47.1° , 60.02° and 67.4°) and peaks of NiAl_2O_4 ($2\theta = 19^\circ$, 31.5° , 36.9° , 59.6° , and 65.9°) can be observed. Once more the main differences between the XRD patterns of the calcined and reduced Ni/LaAl catalyst, are the decreasing intensities of Al_2O_3 and NiAl_2O_4 peaks and the appearance of small peaks of metallic Ni^0 ($2\theta = 44^\circ$ and 51.2°). On the other hand, no diffraction peaks of the La_2O_3 phase were detected in either the calcinated or reduced Ni/

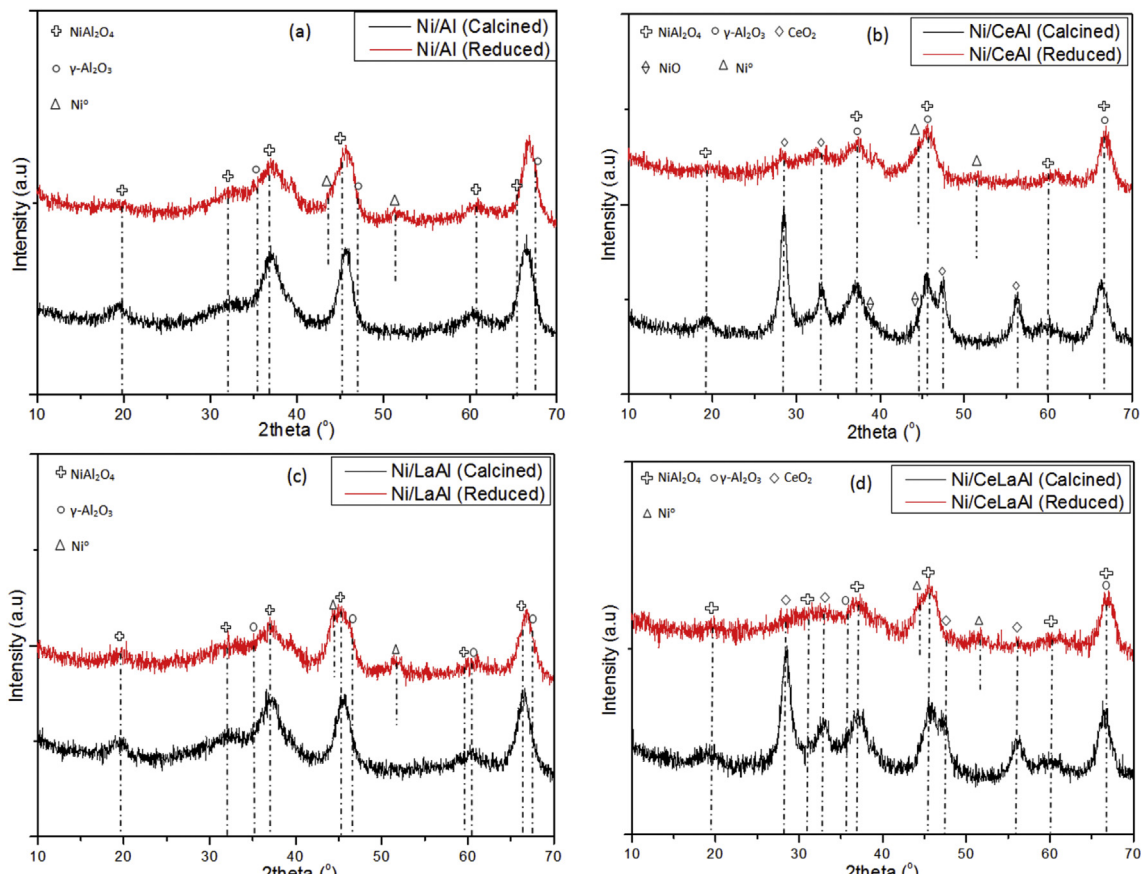


Fig. 2. XRD patterns of calcined and reduced catalysts: (a) Ni/Al, (b) Ni/CeAl, (c) Ni/LaAl, and Ni/CeLaAl catalyst.

LaAl samples. This indicates that either the structure is amorphous or that the La₂O₃ was highly dispersed in the γ -Al₂O₃ (Melchor-Hernández et al., 2013; Garbarino et al., 2015). The possible formation of the compound La₂NiO₄ (NiO–La₂O₃) has also been suggested (Thyssen et al., 2013).

Fig. 2(d) depicts the XRD patterns of the Ni/CeLaAl catalyst after calcination and after reduction. Unlike before, NiO was not identified on the calcined catalyst however, the presence of Ni was confirmed ($2\theta = 44.7^\circ, 52.1^\circ$) on the reduced sample. Moreover, NiAl₂O₄ ($2\theta = 19.3^\circ, 31.5^\circ, 37.2^\circ, 45.2^\circ, 59.7^\circ, 65.9^\circ$, CeO₂ ($2\theta = 28.8^\circ, 33.2^\circ, 47.4^\circ, 56.3^\circ$) and Al₂O₃ ($2\theta = 37.5^\circ, 67^\circ$) have also been observed. As with the Ni/LaAl catalyst no diffraction peaks of the La₂O₃ phase were detected in either the calcinated or reduced Ni/LaAl samples.

The Ni species particle size was determined by XRD measurements (Scherrer analysis) and the results are presented on **Table 5**. A small decrease on the particle size was observed after reduction for all the catalysts, indicating an absence of sintering during the reduction step (Goula et al., 2015). Moreover, it is observed that the Ni/Al sample exhibits the largest mean particle size (16.8 nm for the reduced sample), while the Ni/CeLaAl the smallest (5.1 nm for the corresponding sample). It should be pointed out that it was not possible to estimate the nickel species particle size for the Ni/CeAl catalyst due to an overlapping of the relevant peaks. SEM has been used for the examination of the catalysts surface texture and morphology. **Fig. 3** shows images of the fresh (calcined) and used Ni/Al catalyst, as well as, its carbon mapping (Ia, Ib, and Ic respectively). The Ni/CeAl, Ni/LaAl and Ni/CeLaAl catalysts are also depicted. It is clear that all fresh samples are of different morphology one to another (**Fig. 3**: Ia, IIa, IIIa, and IVa). However, in all cases this morphology includes micro and nano particles, which can be assumed to be either NiO and/or Ni⁰, and larger particles that can be presumed to be alumina (Dou et al., 2014). The examination of the presence of carbon deposits over the catalyst used in the reaction reveals a picture that shows that all catalysts have undergone significant transformation in their morphology; plane particles and others with rugged appearance are shown (**Fig. 3**: Ib, IIb, IIIb, and IVb). It is interesting to note the appearance of various degrees of carbon filaments; for example these appear more intense on the Ni/CeLaAl sample. When carbon quantification is performed (**Fig. 3**: Ic, IIc, IIIc, and IVc), it reveals that in the Ni/Al catalyst, carbon is concentrated on specific areas, most probably those where metallic Ni is to be found; the Ni/CeAl and Ni/LaAl samples reveal an even carbon distribution, while carbon appears most intensely on the Ni/CeLaAl catalyst. In regards to the formation of carbon filaments, it has been suggested that the Ni particles are sintered until a critical size that favors the formation of filamentous carbon, while no filaments will grow below a certain minimum filament diameter (Franchini et al., 2014; Seung-hoon et al., 2014; Zhai et al., 2011).

Carbon filaments have been detected by using an electron microscopy some decades ago (Boehm, 1997; Monthoux and Kuznetsov, 2006; Dresselhaus et al., 2006). In particular, the formation of carbon filaments on the surface of a nickel catalyst during the steam reforming reaction, has been extensively investigated by Baker and his co-workers. Their research work has led to the establishment of a carbon growth mechanism that is widely accepted still today (Baker et al., 1972, 1973). As a matter of fact, the vapor–liquid–solid (VLS) theory that has been developed by Wagner and Ellis in order to explain the Si whiskers growth (Wagner and Ellis, 1964) was adopted by Baker for the carbon filaments growth explanation (Baker et al., 1972). It has been proposed that the VLS mechanism consists of three successive steps. The first one refers to the adsorption of the carbon precursor that is present in the gas phase on the catalytic surface and its dissociation

to elementary carbon atoms formation. The second one is the dissolution of these carbon atoms in the metal and their diffusion through the metallic particle, and the third one is the precipitation of the carbon atoms in the metal – support interface and the formation of a carbon filament.

The structure of the deposited carbon formed onto the different spent catalyst samples was characterized by Raman spectroscopy. It confirms the formation of different carbon structures on the catalyst samples during the reaction, and indicates that the fraction of different carbon types depends on the catalyst-support nature. **Fig. 4** shows the Raman spectra of all catalyst samples resulting in the coke accumulation–formation. From the spectra, two characteristic peaks at around 1344 and 1580 cm⁻¹ respectively can be observed, related to coke formation. These peaks are attributed to the D-band (1344 cm⁻¹) associated with vibrations of carbon atoms with dangling bonds in an amorphous carbon network, and G-band (1580 cm⁻¹) corresponding to the stretching vibration of carbon sp² bonds, which is typically observed in graphitic carbon with high degree of crystallinity, order and symmetry, respectively (Tzounis et al., 2014a, 2014b). The relative intensity of D- divided by G-band (I_D/I_G) can be regarded as a good indicator of the graphitization or the degree of disorder in the carbon structure of the coke formed by the DRM reaction. The smaller I_D/I_G value indicates higher crystallinity due to higher contribution of the graphitized carbon formed (Tzounis et al., 2014c; Liebscher et al., 2013; Wode et al., 2012). The I_D/I_G ratio decreases in the following order: Ni/CeLaAl ($I_D/I_G = 1.59$) > Ni/CeAl ($I_D/I_G = 1.36$) > Ni/LaAl ($I_D/I_G = 1.29$) > NiAl ($I_D/I_G = 1.11$), and it shows that graphitic carbon species decreased with a high I_D/I_G ratio. Therefore, it can be concluded that the Ni/CeLaAl catalyst formulation has the lowest degree of graphitization and it thus effective in suppressing the formation of graphitic carbon, which is a result in good agreement with SEM/EDS results. Specifically, the coke formation on the Ni/CeLaAl, Ni/CeAl and Ni/LaAl catalysts consisted of both amorphous carbon and graphitic carbon species, confirmed by Raman and SEM/EDS. However, the coke formation on these catalysts mainly consisted of the amorphous carbon species, which is easily oxidizable. Moreover, there is no fatal encapsulating carbon species, which causes the deactivation of the catalyst. Thus it is speculated that the addition of ceria or lanthana (or both) as supports helps to accelerate the decomposition/dissociation of CH₄ and CO₂, resulting in increasing formation of a formate intermediate.

4.2. Catalytic activity and selectivity

To test the reproducibility of the experimental results all experiments were repeated at least three times. From these experiments 95% confidence intervals for the mean value were calculated and the results for the Ni/CeAl catalyst in the form of error bars are depicted in **Fig. 5**. As can be seen, individual experimental values lay well within the corresponding confidence intervals showing a very good reproducibility of the repeated experiments.

The theoretical thermodynamic conversion was calculated with the help of the Gibbs Windows 8.0 for Multiphase Equilibrium Calculations part of the HSC Chemistry, Ver. 1.10 program, copyright of Outokumpu Research Oy, Pori, Finland. The values of the theoretical thermodynamic conversions, yields and H₂/CO molar ratio were included in **Fig. 6** along with the experimental results. All pertinent equilibrium calculations were made for the gas mixture containing the main reactants and products of methane dry reforming reaction process considered here, namely CH₄, CO₂, H₂O, CO, H₂, as well as inert gas, He and solid carbon, C(s).

Fig. 6 depicts the influence of reaction temperature on CH₄ and CO₂ conversion, H₂ and CO yield and H₂/CO molar ratio. More specifically, the influence of reaction temperature to methane

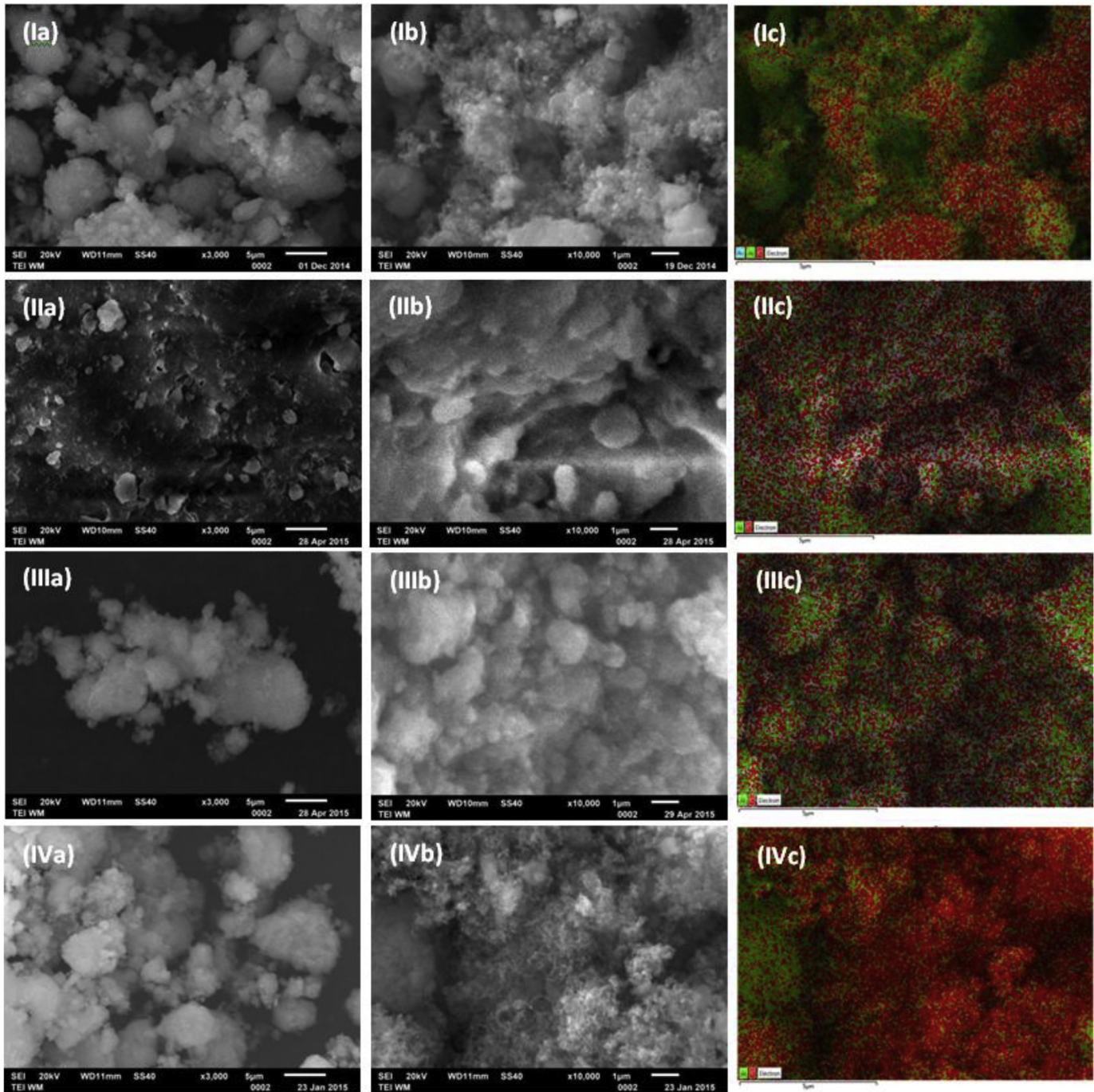


Fig. 3. SEM images of catalysts: (I) Ni/Al, (II) Ni/CeAl, (III) Ni/LaAl, and (IV) Ni/CeLaAl (for all samples: (a) fresh catalyst, (b) used catalyst, (c) carbon mapping of the used catalyst).

(X_{CH_4}) and carbon dioxide (X_{CO_2}) conversion is shown in Fig. 6(a) and (b), respectively. It can be observed that their values increase with temperature, in accordance with the strong endothermic character of the reaction. Moreover, as their molar ratio in the reaction feed was higher than unity ($\text{CH}_4/\text{CO}_2 = 1.5$), it was rather expected that CH_4 conversion would exhibit lower values for the whole temperature range compared with the CO_2 ones. Specifically, for CH_4 its conversion values range from 10% (500 °C) to 70% (800 °C), while for CO_2 from 10% (500 °C) to 90% (800 °C). It can also be observed that Ni supported on modified alumina catalysts are more active than the Ni/Al one, as their CH_4 and CO_2 conversion values were significantly higher (almost by a factor of 2) for the

whole temperature range. On the other hand the Ni/CeAl, Ni/LaAl and Ni/CeLaAl seem to have almost the same catalytic performance concerning reactants conversion, meaning that these catalysts are quite similar in their activity.

Hydrogen and carbon monoxide yields for all the catalysts are shown in Fig. 6(c) and (d), respectively. It can be inferred that H_2 yield values are much higher for the modified alumina supported nickel catalysts compared to the ones for the Ni/Al catalysts (Fig. 6c). Thus, the addition of CeO_2 and/or La_2O_3 in the supporting material improves the performance of all catalysts; however, this improvement is more marked for the Ni/LaAl and Ni/CeLaAl samples, especially for reaction temperatures higher than 625 °C. The

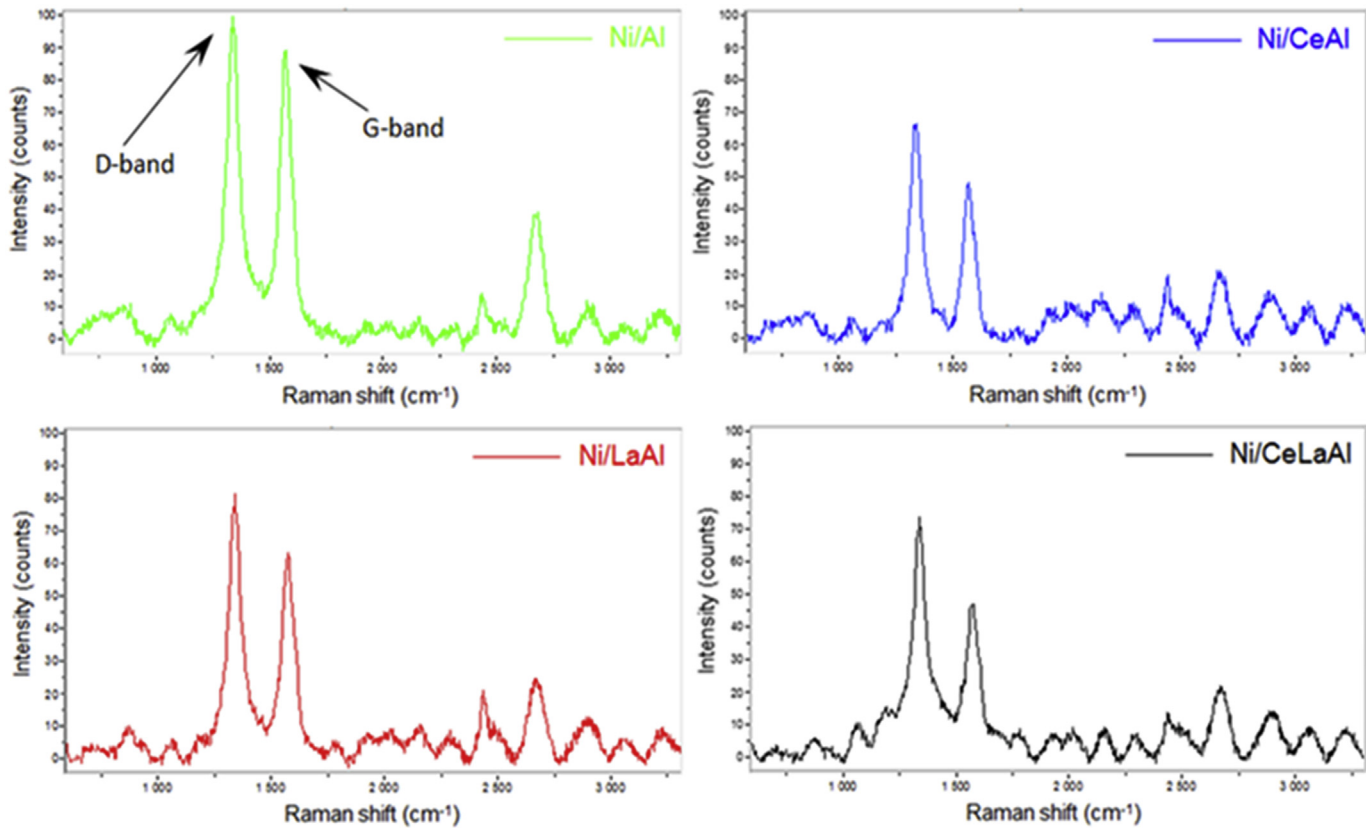
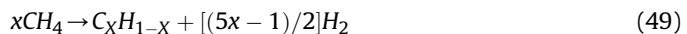


Fig. 4. Raman spectra of the different spent catalyst samples in the range 600–3300 cm⁻¹.

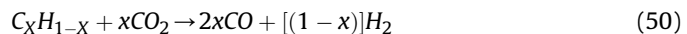
same is true for carbon monoxide yield values i.e., the addition of CeO₂ and/or La₂O₃ leads to higher CO yields compared to the Ni/Al catalyst, but the Ni/CeAl, Ni/LaAl and Ni/CeLaAl have similar performance (Fig. 6d).

Catalytic performance results presented in this work are in accordance with the predictions of reaction thermodynamic analysis by Nikoo et al. (Nikoo and Amin, 2011). They have reported that for CH₄/CO₂ molar ratio in the feed equal to 1.5, the CH₄ conversion values significantly increase with increasing temperature up to 727 °C, while at higher temperatures methane decomposition (Eq. (9)) is considered to be the main reaction forming H₂ and carbon. On the other side, CO₂ acts as a limiting reactant and is not able to convert CH₄ completely, while its conversion values reaches unity (Hong et al., 2001). Moreover at high temperatures, the Reverse Water Gas Shift (RWGS) reaction (Eq. (2)) cannot simultaneously proceed along with the dry reforming reaction and as a result H₂ production increases with increasing temperature. As for the CO, its yield is enhanced in higher temperatures, due to the endothermic character of all the reactions that are involved in its production (Nikoo and Amin, 2011). As has already been mentioned, ceria exhibits extraordinary oxygen storage capacity, which is attributed to the ability of Ce to exist in multiple oxidation states, so that it can participate in redox reactions with the carbon deposited on the catalytic surface (Otsuka et al., 1993). Cerium oxide (CeO₂) redox properties, as well as, its lattice oxygen high mobility resulting in an improved catalytic performance for the hydrocarbon reforming reactions have also been reported by other researchers (Wang and Lu, 1998; Nandini et al., 2005; Natesakhawat et al., 2005; Laosiripojana et al., 2006). The increased carbon resistance of the Ce-promoted catalyst was attributed by Foo et al. (2011) to equilibrium between stable multiple oxidation states of the Ce ion

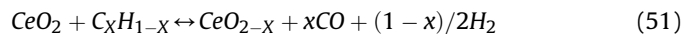
during the reaction; moreover, they concluded that H₂ was probably first produced via CH₄ dehydrogenation into carbonaceous C_xH_{1-x} through:



Subsequent interaction between CO₂ and the carbonaceous deposit yields:



Obviously, there is a limit of 0 ≤ x ≤ 1. Thus, the redox steps involved in the ceria's reduction by unreacted C_xH_{1-x} to CeO_{2-x} and its re-oxidation back to CeO₂ by CO₂ can be described by the following equations:



Concerning ceria's reducibility, it is known that CeO₂ supported on γ-Al₂O₃ is reduced in three main temperature regions. Peaks at low temperature (~773–873 K) correspond to the reduction of surface Ce⁴⁺ of small ceria crystallites. Peaks at intermediate temperature (~900–1100 K) correspond to the reduction of large and bulk ceria crystallites. Peaks at high temperature (>1100 K) correspond to the reduction Ce⁴⁺ → Ce³⁺ of bulk ceria crystallites related to the CeAlO₃ formation. The position of these peaks is strongly dependent on the CeO₂ loading, interaction with γ-Al₂O₃ and particle size (Dresselhaus et al., 2006; Tzounis et al., 2014b; Piras et al., 2005). The hydrogen to carbon monoxide (H₂/CO) molar ratio for all the catalysts at temperature ranging from 500 to 800 °C is shown in Fig. 6(e). It is noteworthy that the H₂/CO ratio

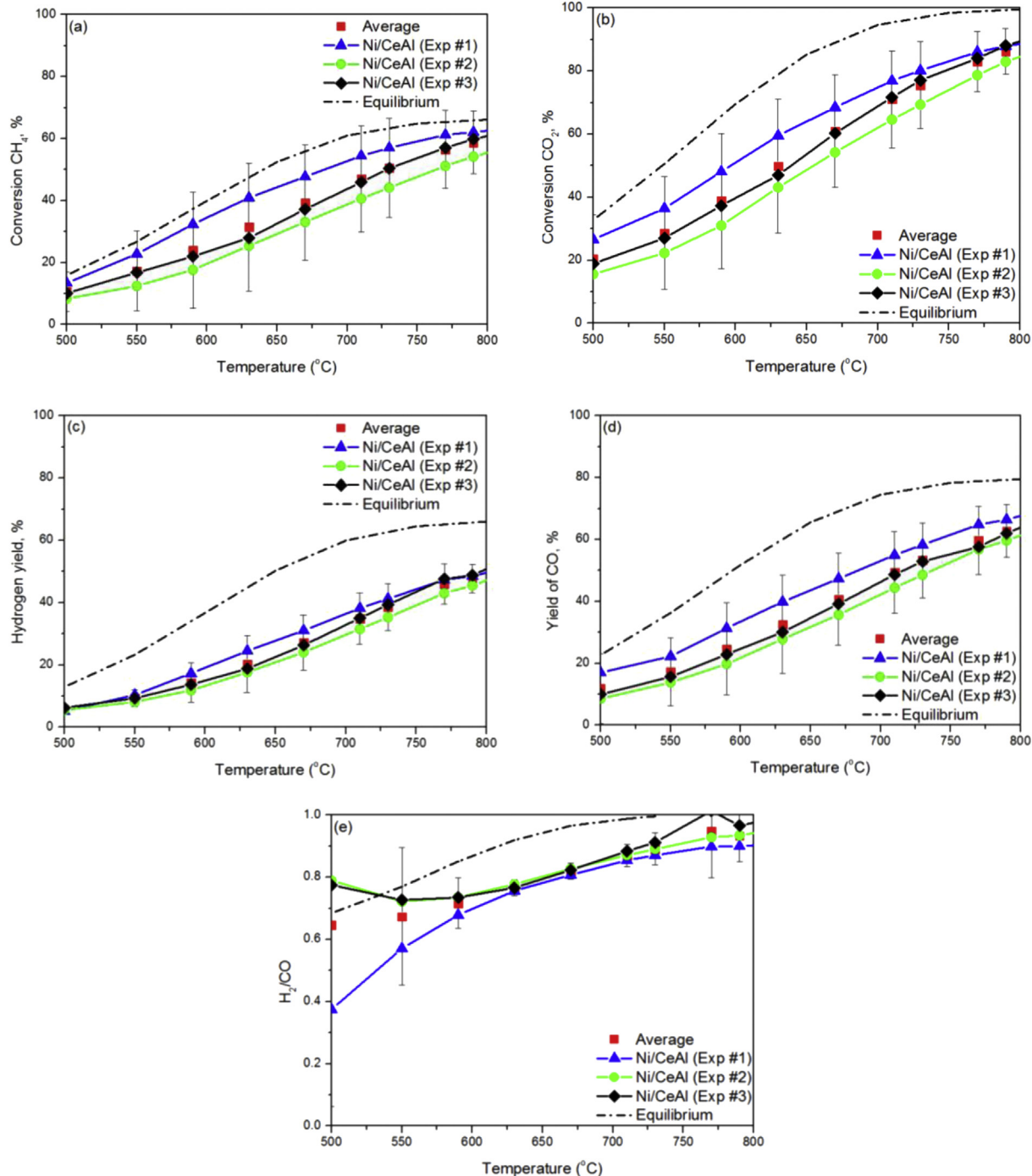


Fig. 5. Repeat experiments for the Ni/CeAl catalyst: (a) Conversion of CH₄ %, (b) Conversion of CO₂ %, (c) H₂ yield %, (d) CO yield %, and (e) H₂/CO Molar ratio [Reaction conditions: WHSV = 120,000 ml g⁻¹ h⁻¹; CH₄:CO₂ = 1.5; P = 1 atm].

increases with increasing temperature, ranging from 0.2 (500 °C) to 0.9 (800 °C) for the Ni/Al, from 0.6 (500 °C) to 0.9 (800 °C) for the Ni/CeAl and from 0.65 (500 °C) to 1.0 (800 °C) for the Ni/LaAl and Ni/CeLaAl catalysts. From Fig. 6(e), it can also be deduced that within the investigated temperature range, the determined H₂/CO molar ratio for the reaction products mixture was below one (1.0); in accordance with the thermodynamic predictions for the specific CH₄ to CO₂ ratio in the feed.

According to Luisetto et al., differences in H₂/CO ratio for the catalysts reflect the differences in the catalytic activity and the

lower reactants conversion yields a lower H₂/CO ratio (Luisetto et al., 2015). In fact the RWGS, which is responsible for the low H₂/CO ratio, is reported to be near equilibrium in the 400–600 °C temperature range (Bradford and Vannice, 1998, 1999). At high temperature the DRM is favored and the CH₄ and CO₂ reactants are converted efficiently. Therefore the smaller amount of CO₂ available for the RWGS gives H₂/CO ratio closer to unity as expected when only the DRM reaction occurs.

As already mentioned, CeO₂ is used as promoter of γ-Al₂O₃ based catalysts because of the combination of the large surface area

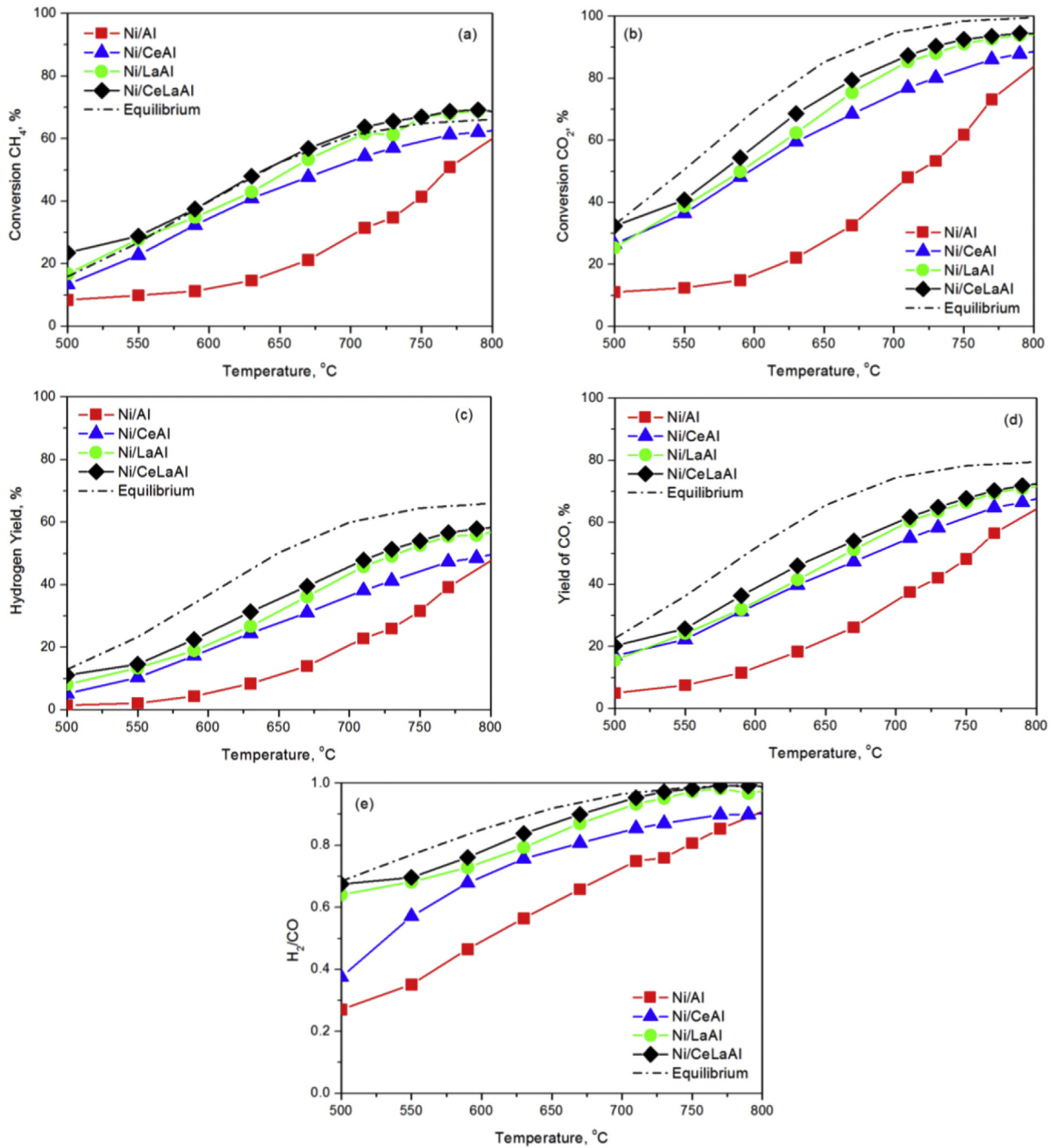
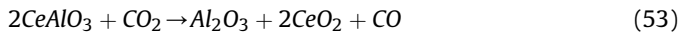


Fig. 6. All catalysts and thermodynamic equilibrium: (a) Conversion of CH₄ %, (b) Conversion of CO₂ %, (c) H₂ yield %, (d) CO yield %, and (e) H₂/CO Molar ratio [Reaction conditions: WHSV = 120,000 ml g⁻¹ h⁻¹; CH₄:CO₂ = 1.5; P = 1 atm].

and stability of γ -Al₂O₃ with the oxygen storage and release capability of CeO₂ (Gonzalez-DelaCruz et al., 2008; Laosiripojana et al., 2005). The promotion of the catalytic performances by CeO₂ addition is also related with the ability to increase the Ni dispersion (Wang and Lu, 1998; Ashok and Kawi, 2013). Moreover, in reducing atmosphere at high temperature, CeO₂ supported on γ -Al₂O₃ reacts to form CeAlO₃-like species (Shyu et al., 1988). As reported by several authors these species play a key role in the removal of carbon residues (Kim et al., 2013). A possible reaction mechanism has been recently proposed by Chen et al. (2013b); the CeAlO₃ formed during catalyst activation or in reaction condition, could react with CO₂ to form CO and CeO₂ (Eq. (53)). CeO₂ oxidizes the CH_x species located at the Ni-support boundary, precursors of

carbonaceous residues, restoring the CeAlO₃ sites (Eq. (54)).



It has also been reported that the significant suppression of carbon deposition is mainly due to the decreasing possibility of the graphene layer formation, as a result of the surface carbon gasification promotion emerging from the CO₂ activation and the Ce³⁺/Ce⁴⁺ cycling (Chen et al., 2013b).

Specifically, a dual path mechanism has been suggested for the CO₂ reforming reaction over reducible oxides; methane (CH₄)

decomposition on the metal active sites followed by reaction with the surface CO₂ species or the adsorbed oxygen atoms derived from CO₂ is involved in one of them (Eq. (55)):



where * denotes a metallic nickel active site or an oxygen vacancy over ceria, while O^{*} denotes adsorbed oxygen species over nickel or an occupied oxygen vacancy (Stagg-Williams et al., 2002).

As for the modified with lanthana nickel catalysts, it has been proven that their improved performance for the reforming reactions can be attributed to the acceleration of the surface CHx species conversion, mainly due to the La₂O₂CO₃ and/or formate species, formed by the CO₂ preferential adsorption on the La₂O₃ support or on the LaO_x species that can decorate the Ni crystallites (Zhang et al., 1996; Slagtern et al., 1997; Verykios, 2003; Verykios et al., 1996).

In the work by Al-Fatesh et al., the effect of using La₂O₃ as promoter and support for Ni/γ-Al₂O₃ catalysts in dry reforming of methane was investigated. It was concluded that addition of La₂O₃ to the catalyst matrix improved the dispersion of Ni and adsorption of CO₂, thus its activity and stability were enhanced (Al-Fatesh et al., 2014). Nanostructured γ-Al₂O₃ with high surface area and mesoporous structure was synthesized by sol-gel method and employed as catalyst support for nickel catalysts in methane reforming with carbon dioxide by Habibi et al. Their catalytic evaluation results showed an increase in methane conversion with increasing lanthanum oxide to 3 mol% and further increase in lanthanum content decreased the catalytic activity (Habibi et al., 2014). Sutthiumporn and Kawi attributed the improved performance of Ni-La₂O₃ catalyst to the presence of a high amount of lattice oxygen surface species which promotes C–H activation in DRM reaction, resulting in high H₂ production. Moreover, they reported that these surface oxygen species catalyst could adsorb CO₂ molecules to form bidentate carbonate species, which can then react with the surface carbon species formed during DRM, resulting in higher CO₂ conversion and lower carbon formation (Sutthiumporn and Kawi, 2011). Yang et al., reported that although the activity of Ni/γ-Al₂O₃ with the La₂O₃ and CeO₂ as promoters was not obviously increased, the carbon deposition on Ni/γ-Al₂O₃ with La₂O₃ and CeO₂ as promoters was greatly suppressed in the CO₂ reforming reaction of CH₄ mainly by preventing the sintering of Ni particles and the dominant formation of the reactive filamentous carbon (Yang et al., 2010).

Fig. 7 shows the conversion of CH₄ (%), CO₂ (%), the yield of H₂ (%), CO (%) and the H₂ to CO molar ratio at 750 °C after 20 h on reaction stream over all catalysts. It can be seen that the performance of the modified with ceria or/and lanthana samples appear to be quite stable. On the contrary, for the Ni/Al sample a drop on all values can be observed, especially after the first 5 h, indicating the presence of inactive “carbon” formed on the catalytic surface with increasing reaction time. For all other samples a smaller drop in conversion values is evidenced, resulting in a drop of H₂ yield by about 5%, 10% and 20% for the Ni/CeLaAl, Ni/LaAl and Ni/CeAl catalysts, respectively (Fig. 7c). According to the literature, (Makri et al., 2016) these results could suggest that the relatively small drop of H₂-yield (%) after 20 h of dry reforming is due either to morphological/structural changes of the Ni and support phases (partial loss of active catalytic sites on Ni and the Ni-support interface) or to the removal of inactive “carbon” via hydrogenation.

4.3. Theoretical results

The estimated parameter values (i.e., effectiveness factors and

DRM kinetics parameters) are summarized on Table 6. Estimated parameter values present a consistency in catalysts activity towards higher activity when going from the Ni/Al catalyst to those doped with Ce, La and both. In general, doped catalysts have higher activity and smaller activation energy. As for the prevailing reactions, SRM2 is of negligible importance, whereas SRM1 has a small but discernible contribution to the overall reaction. Also, it is evident that methane dry reforming is accompanied by reverse WGS to a limited but important degree. RWGS produces the small quantities of steam necessary to maintain simultaneous steam reforming, mainly by small SRM1 reactivity. As it concerns the main DRM reaction its reaction rate increases by several orders of magnitude by increasing temperature from 500 °C to 800 °C. Moreover its effectiveness factor takes on values close to unity for all catalysts. This is direct evidence that internal (intraparticle) mass and heat transfer limitations are of minor importance for the main reaction of the process and the size of catalysts used here. The same conclusion holds for the WGS reaction. However, internal (intraparticle) mass and heat transfer limitations are of some importance for SRM1 and SRM2 reactions, for the Ni/Al and Ni/CeAl catalysts. This important matter will be clarified below.

Fig. 8, presents a direct comparison between the experimentally attained values of CH₄ and CO₂ conversion and H₂ and CO yield and the values predicted theoretically. The theoretical reactor model incorporated the estimated values of effectiveness factors and DRM kinetics parameters given in Table 6. The agreement between experimental and theoretical results is fairly good for conversion values and excellent for yield values. The small discrepancy between experimental results and model predictions in regards to conversion values for the modified alumina catalysts, for temperatures exceeding 700 °C, can be attributed, on one hand, to side reactions taking place at higher temperatures, which would be difficult to include in any theoretical model and on the other hand, to the influence of internal (intraparticle) mass and heat transfer limitations, which are more pronounced at higher temperatures and for the catalysts containing ceria.

To delineate the relative importance of external (interparticle) and internal (intraparticle) mass and heat transport phenomena on the experimental and theoretical outcomes, Mears criteria (Eq. 56a,b) for interfacial mass and heat transfer as well as Weisz-Prater criterion (Eq. (57)) for intraparticle diffusion were applied with the help of the theoretical model also applied onto catalytic conditions resembling those of the real catalytic system for the catalysts and the type of reactor used in the present study.

$$\frac{\sum_{j=1}^{N_R} \nu_{ij} R_j(c_i, P, T) \rho_B d_P n}{2k_{m,i} c_i} < 0.15 \quad (56a)$$

$$\left| \frac{\sum_{ij=1}^{N_R} \eta_j (-\Delta H_{Rj}) R_j(c_i, P, T) \rho_S d_P E_{aj}}{2h g T^2 R} \right| < 0.15 \quad (56b)$$

$$\frac{\sum_{j=1}^{N_R} \nu_{ij} R_j(c_i, P, T) \rho_S d_P^2}{4D_{eff,i} c_i^S} < < 1 \quad (57)$$

where, ρ_S is the density of the solid catalyst.

Fig. 9 depicts the Weisz-Prater parameter, C_{WP}, applied to the Ni/Al catalyst, for two temperature limiting values, 500 and 800 °C, for the main reactants of the reactive system, CH₄, CO₂ and H₂, along the reactor length. C_{WP} is much higher at the higher temperature than at the lower one and in all cases it is much larger than unity, attaining even larger values at 800 °C. Under such conditions,

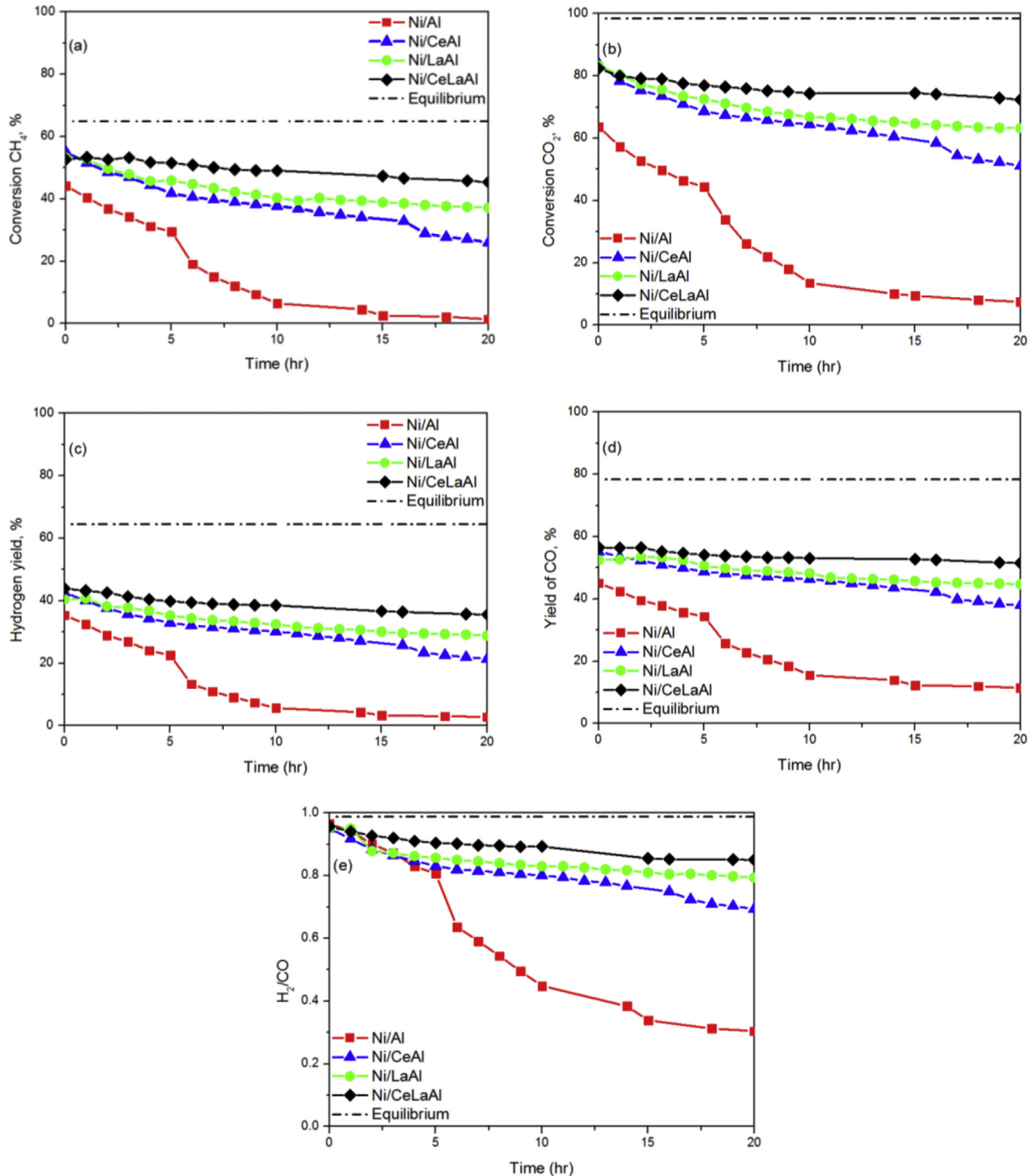


Fig. 7. Stability tests: (a) Conversion of CH₄, %, (b) Conversion of CO₂, %, (c) H₂ yield, %, (d) CO yield, %, and (e) H₂/CO Molar ratio [Reaction conditions: WHSV = 120,000 ml g⁻¹ h⁻¹; CH₄:CO₂ = 1.5; P = 1 atm, T = 750 °C, t = 20 h].

Table 6

Estimated parameter values (effectiveness factors and DRM kinetic parameters).

Parameter	Ni/Al	Ni/CeAl	Ni/LaAl	Ni/CeLaAl
η_1	$1.086 \cdot 10^{-2}$	$2.114 \cdot 10^{-2}$	$1.780 \cdot 10^{-1}$	1.0
η_2	0.0	0.0	1.0	1.0
η_3	1.0	1.0	1.0	1.0
η_4	1.0	$9.013 \cdot 10^{-1}$	$9.972 \cdot 10^{-1}$	1.0
k_{DRM} (mol/Kg _{cat} s bar ²)	$1.361 \cdot 10^4$	$1.027 \cdot 10^5$	$2.397 \cdot 10^4$	$1.644 \cdot 10^5$
E_a DRM (J/mol)	$4.667 \cdot 10^5$	$2.268 \cdot 10^5$	$1.784 \cdot 10^5$	$1.899 \cdot 10^5$

overall reaction rates are significantly limited by intraparticle diffusion. For CO₂ at the lower temperature value, 500 °C, C_{WP} becomes less than unity (<0.3) and under such conditions it is expected that intraparticle diffusion becomes less prominent. Using catalysts with smaller particle size would diminish the influence of intraparticle diffusion on overall reaction rates.

Fig. 10(a) depicts the Mears parameter, C_{M-m}, for interfacial mass transfer, calculated for the same chemical species and experimental conditions as used previously for the Weisz-Prater criterion, whereas Fig. 10(b) and (c), depict bulk and particle

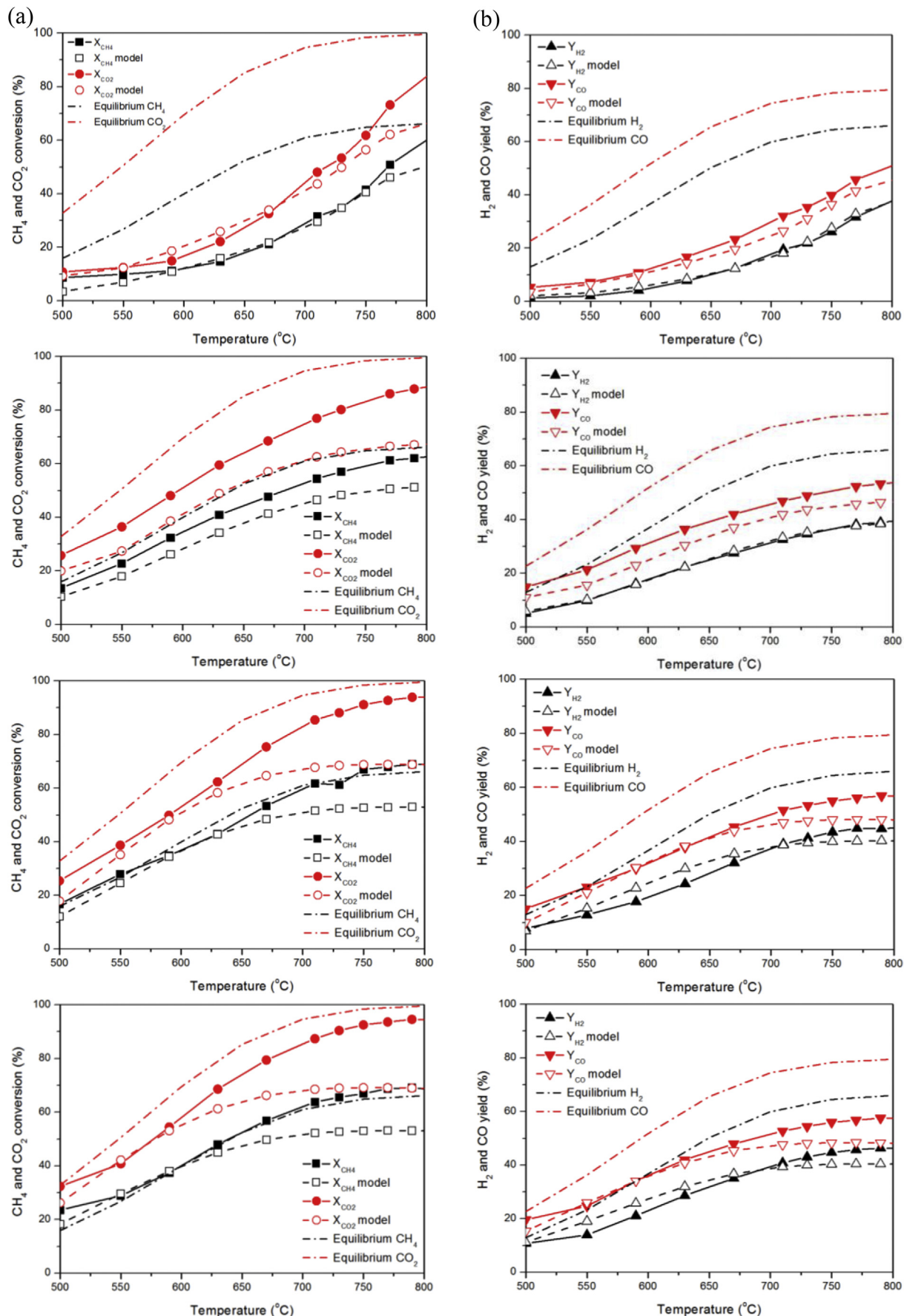


Fig. 8. Experimental values and reactor model calculations for the catalysts (from top to bottom): 8Ni/Al, 8Ni/CeAl, 8Ni/LaAl and 8Ni/CeLaAl. For all samples: (a) CH₄ and CO₂ conversions, (b) H₂ and CO yield [Experimental reaction conditions: WHSV = 120,000 ml g⁻¹ h⁻¹; CH₄:CO₂ = 1.5; P = 1 atm].

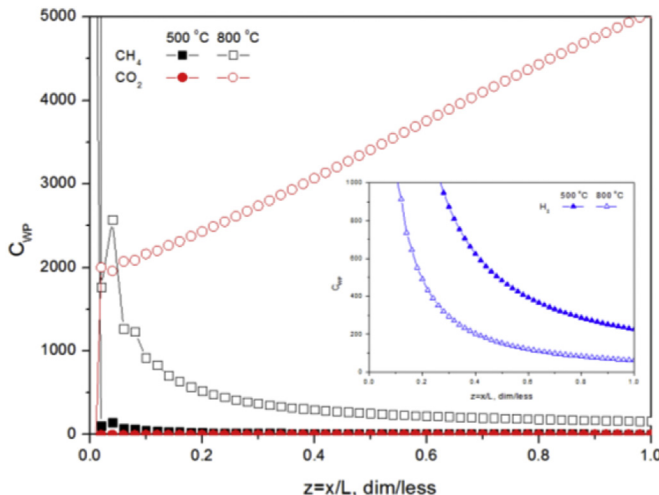


Fig. 9. Weisz-Prater criterion for the Ni/Al catalyst.

surface concentrations of the same chemical species, at 500 °C and 800 °C, respectively. Where C_{M-m} attains high values, higher than unity, interfacial mass transfer is important and surface concentration of that species differs substantially from its bulk concentration. Again, interfacial mass transfer limitations become more significant at the highest temperature value, and at the same time differences between bulk and surface concentrations of the chemical species become larger. On the other hand, at the lowest temperature, 500 °C, C_{M-m} takes on relatively smaller values and differences between species bulk and surface concentrations become relatively confined, except for H_2 , for which large values of C_{M-m} were reflected on significantly different concentration values in the bulk and on the particle surface.

In Fig. 10(d), C_{M-h} values of Mears parameter for interfacial heat transfer were depicted for each one of the prevailing reactions assumed in the present study, for the same catalyst and at the same experimental conditions that were used previously, whereas Fig. 10(e) depicts the corresponding bulk and surface temperature values. At the lowest temperature, 500 °C, C_{M-h} remains less than 0.15, for all reactions, indicating negligible influence of heat transfer limitations and for that reason bulk and particle surface temperatures become almost identical. On the other hand, at the highest temperature, 800 °C, C_{M-h} is greater than 0.15, indicating significant influence of interfacial heat transfer limitations, and for that bulk and surface temperature remain different along reactor length. Moreover, isothermal conditions imposed throughout all experiments conducted in the present study are reflected in the constant bulk temperature along the whole reactor length, whereas endothermicity of the overall reaction is reflected on particle surface temperature which is lower than the bulk temperature, everywhere along the reactor length.

Finally, Fig. 11 depicts three other important variables, namely gas mixture total molar flux, bulk total molar concentration and superficial velocity, as calculated by the theoretical model along the reactor length. Non ideality and compressibility of the gaseous reactant mixture were taken explicitly into account in the model and this permitted the evaluation of the physicochemical properties of the gas mixture at the varying thermal and pressure conditions along the reactor length. Bulk total molar concentration, c , remains almost constant throughout the reactor (it diminishes indiscernibly), whereas total molar flux, N , i.e. total flow rate, increases slightly in all cases, due to the stoichiometry of the overall reaction. On the other hand, superficial velocity, v , increases

significantly from the reactor inlet to outlet, at the highest temperature. In all cases, total and species flow rates increase insignificantly from inlet to outlet conditions at the experimental conditions used in the present study and therefore measurement of them at the inlet conditions suffices for an accurate determination of them.

5. Conclusions

A number of nickel, supported on un-promoted and promoted with CeO_2 , La_2O_3 , and $\text{CeO}_2-\text{La}_2\text{O}_3$, alumina catalysts were tested for the biogas dry reforming reaction. Although the Ni/CeAl , Ni/LaAl and Ni/CeLaAl have significantly enhanced catalytic performance concerning reactants conversion compared to the Ni/Al catalyst, they are also quite similar in their activity. Moreover, stability tests showed that the modified alumina catalysts could maintain their activity for over 20 h, whilst the Ni/Al catalyst was stable for only up to 5 h of operation. Having said that, catalysts containing lanthanum (i.e., Ni/LaAl and Ni/CeLaAl) perform marginally better than the sample containing only ceria (Ni/CeAl).

The participation of Ce and La in redox reactions with the surface deposited carbon, due to their high oxygen storage capacity enabling them to exist in multiple oxidation states is the main reason for the improved DRM catalytic performance of the modified with ceria and/or lanthana nickel catalysts.

A theoretical reactor model has been developed herein. Posterior Bayesian parameter estimation procedure permitted the estimation of the appropriate effectiveness factors, which replaced internal mass and heat transfer limitations, and DRM kinetics parameters. Application of the model for the conditions used in the experiments permitted the gaining of additional insight of the overall reaction process. Good agreement between experimental and theoretical results was obtained. Application of the model in calculating Weisz Prater and Mears criteria parameters helped to identify the range of experimental conditions where results were limited by significant mass and heat transfer limitations. Such estimations would facilitate the development of reactor models for up scaling to pilot and industrial scale reactors.

Appendix A. Multiresponse Bayesian Parameter Estimation

For multiresponse data, GREGPLUS computes modal and interval estimates of the parameters using a user-provided matrix of multiresponse observations by using the objective function,

$$\Phi(\boldsymbol{\theta}) = \sum_{b=1}^B (n_b + m_b + 1) \ln |\mathbf{v}_b(\boldsymbol{\theta})| \quad (\text{A.1})$$

based on a user-selected arrangement of the responses into one or more blocks ($b=1, \dots, B$), where n and m are the number of events and working responses in block b , respectively (Stewart et al., 1992), and $|\mathbf{v}_b(\boldsymbol{\theta})|$ is the determinant of the residual matrix defined below. From each block b , GREGPLUS selects m working responses whose weighted deviations from the current model, given by $[y_{ij} - f_{ij}(\boldsymbol{\theta})] \sqrt{w_{ij}}$, are linearly independent over the events, where $y_{ij}, f_{ij}(\boldsymbol{\theta})$ and w_{ij} are the observation, model prediction and user-provided weight for response i in event j , respectively. Then, each block sub-matrix function $\mathbf{v}_b(\boldsymbol{\theta})$ with elements

$$v_{bik}(\boldsymbol{\theta}) = \sum_{j=1}^n \sqrt{w_{ij} w_{kj}} [y_{ij} - f_{ij}(\boldsymbol{\theta})] [y_{kj} - f_{kj}(\boldsymbol{\theta})] \quad (\text{A.2})$$

where n is the number of events in the data set, has a positive determinant over the investigated range of $\boldsymbol{\theta}$, as equation (A.1)

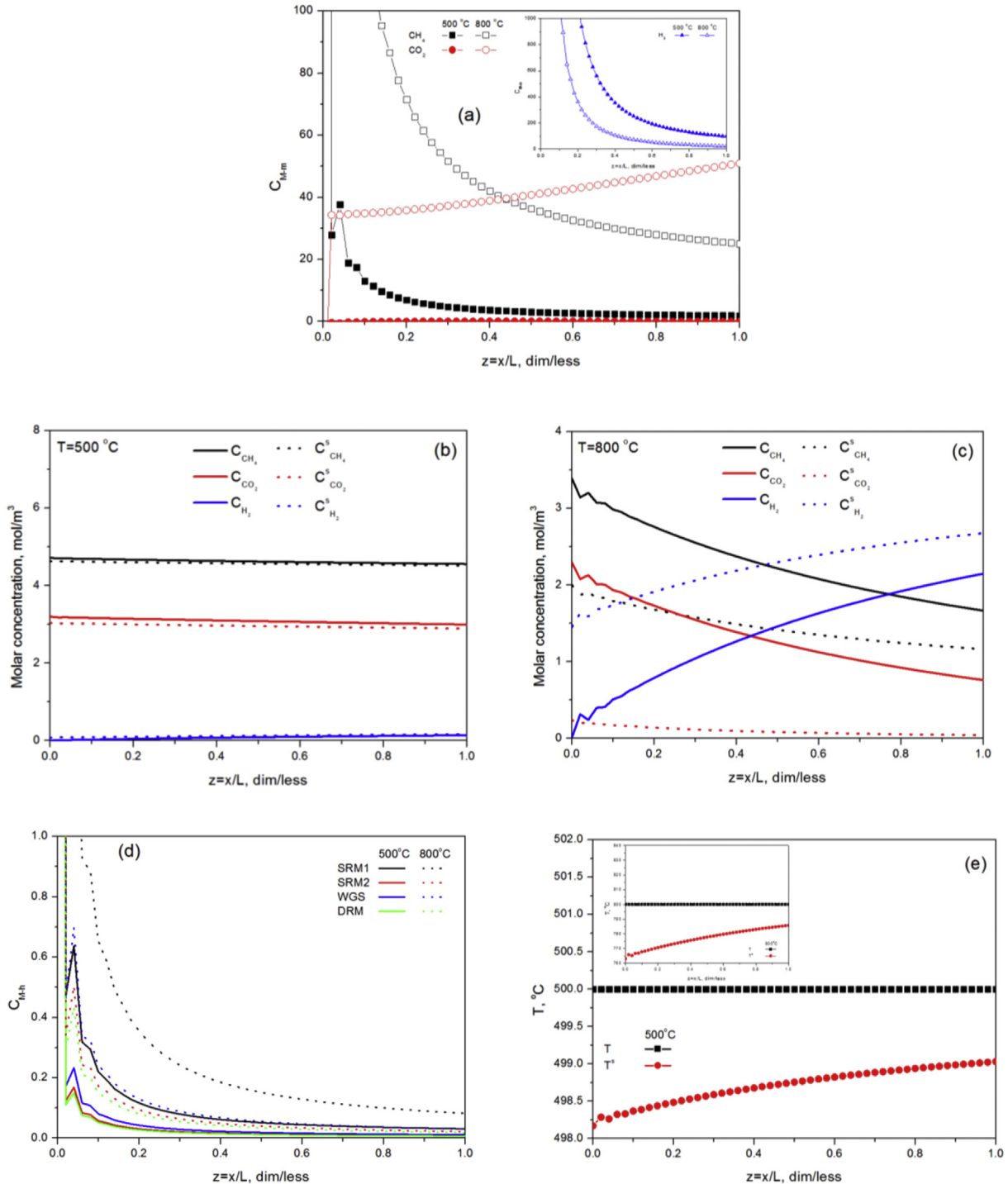


Fig. 10. (a) Mears criteria for interfacial mass transfer, (b) & (c) Bulk and surface concentration distribution along the reactor length at 500 and 800 °C, respectively, (d) Mears criteria for interfacial heat transfer, (e) Bulk and surface temperature distribution along the reactor length at 500 and 800 °C [All figures refer to the Ni/Al catalyst].

requires. Note that the dependent variable y_i or f_i represents $X_{CH_4}, X_{CO_2}, Y_{CO}, Y_{H_2}$ for the index values $i=1,2,3,4$, respectively.

The objective function is expanded as a quadratic function of the parameters, around the initial guesses of the current iteration (Stewart et al., 1992). The parametric sensitivities needed for this step can be generated by GREGPLUS with optimized divided-difference steps; alternatively, some or all of them can be provided by the user's subroutine. The resulting minimization problem is solved with successive quadratic programming, starting from the

user's guesses for the parameters and using a modified Gauss-Jordan algorithm, within a user-defined feasible region; then, a weak line search is conducted to establish an improved objective value and initial parameter vector for the next iteration. Ill-conditioned solutions are avoided by using a threshold value for acceptance of pivotal divisors in the quadratic minimization calculations. Termination of the iteration is controlled by the current quadratic programming predictions of the correction vector. Interval estimates for the individual estimated parameters are then

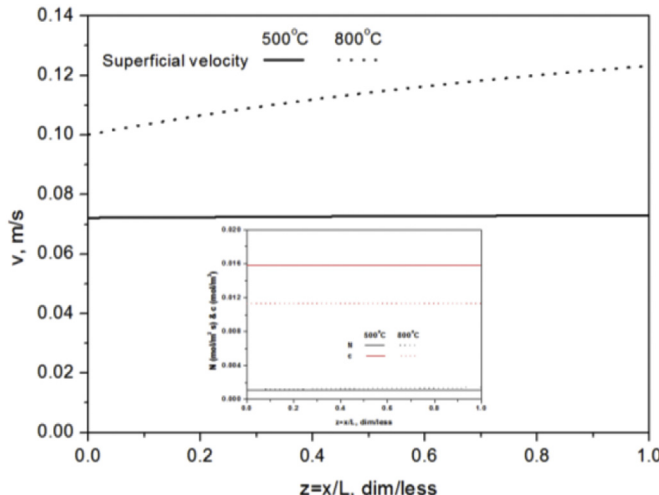


Fig. 11. Superficial gas velocity, Total molar flux (inset) and Total molar concentration (inset) along the reactor length at 500 and 800 °C for the Ni/Al catalyst.

calculated from the final quadratic expansion of the objective functions. Both codes PDAPLUS and GREGPLUS are written in FORTRAN and are properly incorporated as subroutines in a user-defined code which is written in Athena Visual Workbench (AVW) language and translated automatically to Fortran by ATHENA. All information above was given also elsewhere (Tsakiroglou et al., 2003; Avraam et al., 2010) from where it was taken and adapted to the present problem.

References

- Aghamohammadi, S., Haghghi, M., Karimipour, S., 2013. A comparative synthesis and physicochemical characterizations of Ni/Al₂O₃-MgO nanocatalyst via sequential impregnation and sol-gel methods used for CO₂ reforming of methane. *J. Nanosci. Nanotechnol.* 13, 4872–4882.
- Al-Fatesh, A.S., Naeem, M.A., Fakeeha, A.H., Abasaeed, A.E., 2014. Role of La₂O₃ as promoter and support in Ni/γ-Al₂O₃ catalysts for dry reforming of methane. *Chin. J. Chem. Eng.* 22, 28–37.
- Almeida, P., Silva, P.D., 2009. The peak of oil production: timings and market recognition. *Energy Policy* 37, 1267–1276.
- Ang, B.W., Choong, W.L., Ng, T.S., 2015. Energy security: definitions, dimensions and indexes. *Renew. Sustain. Energy Rev.* 42, 1077–1093.
- Angelis, S.D., Monteleone, G., Giacconi, A., Lemonidou, A.A., 2013. Low temperature methane steam reforming: catalytic activity and coke deposition study. *Chem. Eng. Trans.* 35, 1201–1206.
- Ashok, J., Kawi, S., 2013. Steam reforming of toluene as a biomass tar model compound over CeO₂ promoted Ni/CeO₂-Al₂O₃ catalytic systems. *Int. J. Hydrogen Energy* 38, 13938–13949.
- Avraam, D.G., Halkides, T.I., Liguras, D.K., Bereketidou, O.A., Goula, M.A., 2010. An experimental and theoretical approach for the biogas steam reforming reaction. *Int. J. Hydrogen Energy* 35 (18), 9818–9827.
- Baker, R.T.K., Barber, M.A., Harris, P.S., Feates, F.S., Waite, R.J., 1972. Nucleation and growth of carbon deposits from the nickel catalyzed decomposition of acetylene. *J. Catal.* 26, 51–62.
- Baker, R.T.K., Harris, P.S., Thomas, R.B., Waite, R.J., 1973. Formation of filamentous carbon from iron, cobalt and chromium catalyzed decomposition of acetylene. *J. Catal.* 30, 86–95.
- Bereketidou, O.A., Goula, M.A., 2012. Biogas reforming for syngas production over nickel supported on ceria-alumina catalysts. *Catal. Today* Special Issue Catal. Biorefin. 195, 93–100.
- Boehm, H.P., 1997. The first observation of carbon nanotubes. *Carbon* 35, 581–584.
- Bradford, M.C.J., Vannice, M.A., 1998. CO₂ reforming of CH₄ over supported Pt catalysts. *J. Catal.* 173, 157–171.
- Bradford, M.C.J., Vannice, M.A., 1999. CO₂ reforming of CH₄. *Catal. Rev.* 41, 1–42.
- Charisiou, N.D., Goula, M.A., 2014. Attitudes of Greek university students towards energy and the environment. *Glob. Nest J.* 16, 856–865.
- Chen, Wei, Zhao, Guofeng, Xue, Qingsong, Chen, Li, Lu, Yong, 2013a. High carbon-resistance Ni/CeAlO₃-Al₂O₃ catalyst for CH₄/CO₂ reforming. *Appl. Catal. B Environ.* 136–137, 260–268.
- Chen, W., Zhao, G., Xue, Q., Chen, L., Lu, Y., 2013b. High carbon-resistance Ni/CeAlO₃-Al₂O₃ catalyst for CH₄/CO₂ reforming. *Appl. Catal. B Environ.* 136–137, 260–268.
- de Sousa, H.S.A., da Silva, A.N., Castro, A.J.R., Campos, A., Filho, J.M., Oliveira, A.C., 2012. Mesoporous catalysts for dry reforming of methane: correlation between structure and deactivation behaviour of Ni-containing catalysts. *Int. J. Hydrogen Energy* 37, 12281–12291.
- Dibbern, H.C., Olesen, P., Rostrup-Nielsen, J.R., Tøttrup, P.B., 1986. *Hydrocarb. Process* 65, 71.
- Djinović, P., Osojnik Črnivec, I.G., Erjavec, B., Pintar, A., 2012. Influence of active metal loading and oxygen mobility on coke-free dry reforming of Ni-Co bimetallic catalysts. *Appl. Catal. B Environ.* 125, 259–270.
- Dou, B., Wang, C., Song, Y., Chen, H., Xu, Y., 2014. Activity of Ni-Cu-Al based catalyst for renewable hydrogen production from steam reforming of glycerol. *Energy Convers. Manag.* 78, 253–259.
- Dresselhaus, M.S., Dresselhaus, G., Eklund, P.C., 2006. *Science of Fullerenes and Carbon Nanotubes*. Academic Press, San Diego.
- Foo, S.Y., Cheng, C.K., Nguyen, T.-H., Adesina, A., 2011. Kinetic study of methane CO₂ reforming on Co-Ni/Al₂O₃ and Ce-Co-Ni/Al₂O₃ catalysts. *Catal. Today* 164, 221–226.
- Franchini, C.A., Aranzaes, W., de Farias, A.M.D., Pecchi, G., Fraga, M.A., 2014. Cerium-substituted LaNiO₃ mixed oxides as catalyst precursors for glycerol steam reforming. *Appl. Catal. B Environ.* 147, 193–202.
- Garbarino, G., Wang, C., Valsamakis, I., Chitsazan, S., Riani, P., Finocchio, E., Flytzani-Stephanopoulos, M., Busca, G., 2015. A study of Ni/Al₂O₃ and Ni-La/Al₂O₃ catalysts for the steam reforming of ethanol and phenol. *Appl. Catal. B Environ.* 174, 21–34.
- Gonzalez-DelaCruz, V., Holgado, J., Pereniguez, R., Caballero, A., 2008. Morphology changes induced by strong metal-support interaction on a Ni-ceria catalytic. *J. Catal.* 257, 307–314.
- Goula, M.A., Lemonidou, A.A., Efstratiou, A.M., 1996. Characterization of carbonaceous species formed during reforming of CH₄ with CO₂ over Ni/CeO₂-Al₂O₃ catalysts studied by various transient techniques. *J. Catal.* 161, 626–640.
- Goula, M.A., Bereketidou, O.A., Papageridis, K.N., Charisiou, N.D., 15–20 June, 2014. Influence of the preparation procedure parameters on the performance of Ni/γ-alumina catalysts for the biogas reforming reaction. In: Proc. Int. Conf. On World Hydrogen Energy Conference, Gwangju: South Korea, pp. 1435–1441.
- Goula, M.A., Charisiou, N.D., Papageridis, K.N., Delimitis, A., Pachatouridou, E., Iliopoulos, E.F., 2015. Nickel on alumina catalysts for the production of hydrogen rich mixtures via the biogas dry reforming reaction: influence of the synthesis method. *Int. J. Hydrogen Energy* 40, 9183–9200.
- Habibi, N., Rezaei, M., Majidian, N., Andache, M., 2014. CH₄ reforming with CO₂ for syngas production over La₂O₃ promoted Ni catalysts supported on mesoporous nanostructured γ-Al₂O₃. *J. Energy Chem.* 23, 435–442.
- Hong, S.W., Oh, S.M., Park, D.W., Kim, G.J., 2001. The methane reforming with carbon dioxide on Ni-catalyst activated by a DC-pulsed corona discharge. *Ind. Eng. Chem.* 7, 410–416.
- Jun, H.J., Park, M.J., Baek, S.C., Bae, J.W., Ha, K.S., Jun, K.W., 2011. Kinetics modeling for the mixed reforming of methane over Ni-CeO₂/MgAl2O4. *J. Nat. Gas Chem.* 20, 9–17.
- Kim, T.Y., Kim, S.M., Lee, W.S., Woo, S.I., 2013. Effect and behavior of cerium oxide in Ni/γ-Al₂O₃ catalysts on autothermal reforming of methane: CeAlO₃ formation and its role on activity. *Int. J. Hydrogen Energy* 38, 6027–6032.
- Koh, A.C.W., Chen, L., Leong, W.K., Johnson, B.F.G., Khimyak, T., Lin, J., 2007. Hydrogen or synthesis gas production via the partial oxidation of methane over supported nickel-cobalt catalysts. *Int. J. Hydrogen Energy* 32, 725–730.
- Koo, K.Y., Lee, S.-H., Jung, U.H., Roh, H.-S., Yoon, W.L., 2014. Syngas production via combined steam and carbon dioxide reforming of methane over Ni-Ce/MgAl₂O₄ catalysts with enhanced coke resistance. *Fuel Process. Technol.* 119, 151–157.
- Laosiripojana, N., Sutthiripak, W., Assabumrungrat, S., 2005. Synthesis gas production from dry reforming of methane over CeO₂ doped Ni/Al₂O₃: influence of the doping ceria on the resistance toward carbon formation. *Chem. Eng.* 112, 13–22.
- Laosiripojana, N., Sangtongkitcharoen, W., Assabumrungrat, S., 2006. Catalytic steam reforming of ethane and propane over CeO₂-doped Ni/Al₂O₃ at SOFC temperature: improvement of resistance toward carbon formation by the redox property of doping CeO₂. *Fuel* 85, 323–332.
- Lemonidou, A.A., Goula, M.A., Vasalos, I.A., 1998. Carbon dioxide reforming of methane over 5 wt. % nickel calcium aluminate catalysts – effect of preparation method. *Catal. Today* 46, 175–183.
- Liebscher, M., Tzounis, L., Pötschke, P., Heinrich, G., 2013. Influence of the viscosity ratio in PC/SAN blends filled with MWCNTs on the morphological, electrical, and melt rheological properties. *Polymer* 54, 6801–6808.
- Liu, Z.-W., Roh, H.-S., Jun, K.-W., 2003. Carbon dioxide reforming of methane over Ni/Al₂O₃/Al₂O₃. *J. Ind. Eng. Chem.* 9, 267–274.
- Liu, C., Ye, J., Jiang, J., Pan, Y., 2011. Progresses in the preparation of coke resistant Ni-based catalyst for steam and CO₂ reforming of methane. *ChemCatChem* 3, 529–541.
- Lu, Y., Chen, J.C., Liu, Y., Xue, Q.S., He, M.Y., 2008. Highly sulfur-tolerant Pt/Ce_{0.8}Gd_{0.2}O_{1.9} catalyst for steam reforming of liquid hydrocarbons in fuel cell applications. *J. Catal.* 254, 39–48.
- Luisetto, I., Tuti, S., Battocchio, C., Mastro, S.L., Sodo, A., 2015. Ni/CeO₂-Al₂O₃ catalysts for the dry reforming of methane: the effect of CeAlO₃ content and nickel crystallite size on catalytic activity and coke resistance. *Appl. Catal. A General* 500, 12–22.
- Makri, M.M., Vasilides, M.A., Petalidou, K.C., Efstratiou, A.M., 2016. Effect of support composition on the origin and reactivity of carbon formed during dry reforming of methane over 5 wt% Ni/Ce_{1-x}MxO_{2-δ} (M = Zr⁴⁺, Pt³⁺) catalysts. *Catal. Today* 259, 150–164.

- Martínez, R., Romero, R., Guimon, C., Bilbao, R., 2004. CO₂ reforming of methane over coprecipitated Ni-Al catalysts modified with lanthanum. *Appl. Catal. A* General 274, 139–149.
- Mathews, A.P., 2014. Renewable energy technologies: panacea for world energy security and climate change? *Procedia Comput. Sci.* 32, 731–737.
- Melchor-Hernández, C., Gómez-Cortés, C., Díaz, G.A., 2013. Hydrogen production by steam reforming of ethanol over nickel supported on La-modified alumina catalysts prepared by sol-gel. *Fuel* 107, 828–835.
- Monthoux, M., Kuznetsov, V.L., 2006. Who should be given the credit for the discovery of carbon nanotubes? *Carbon* 44, 1621–1623.
- Morterra, C., Bolis, V., Magnacca, G., 1996. Surface characterization of modified aluminas .4. surface hydration and lewis acidity of CeO₂-Al₂O₃ systems. *J. Chem. Soc. Faraday Trans.* 92, 1991–1999.
- Nandini, A., Pant, K.K., Dhingra, S.C., 2005. K-, CeO₂-, and Mn-promoted Ni/Al₂O₃ catalysts for stable CO₂ reforming of methane. *Appl. Catal. A* General 290, 166–174.
- Natesakhwat, S., Oktar, O., Ozkan, U.S., 2005. Effect of lanthanide promotion on catalytic performance of sol-gel Ni/Al₂O₃ catalysts in steam reforming of propane. *J. Mol. Catal. A Chem.* 241, 133–146.
- Ni, J., Chen, L., Lin, J., Kawi, S., 2012. Carbon deposition on borated alumina supported nanosized Ni catalysts for dry reforming of CH₄. *Nano Energy* 1, 674–686.
- Nikoo, M.K., Amin, N.A.S., 2011. Thermodynamic analysis of carbon dioxide reforming of methane in view of solid carbon formation. *Fuel Process. Technol.* 92, 678–691.
- Odedairo, T., Chen, J., Zhu, Z., 2013. Metal-support interface of a novel Ni-CeO₂ catalyst for dry reforming of methane. *Catal. Commun.* 31, 25–31.
- Olsbye, U., Wurzel, T., Mleczko, L., 1997. Kinetic and reaction engineering studies of dry reforming of methane over a Ni/Al₂O₃ catalyst. *Ind. Eng. Chem. Res.* 36, 5180–5188.
- Osaki, T., Masuda, H., Mori, T., 1994. Intermediate hydrocarbon species for the CO₂-CH₄ reaction on supported Ni catalysts. *Catal. Lett.* 29, 33–37.
- Osuka, K., Ushiyama, T., Yamanaka, I., 1993. Partial oxidation of methane using the redox of cerium oxide. *Chem. Lett.* 22, 1517.
- Pino, Lidia, Vita, Antonio, Lagana, Massimo, Recupero, Vincenzo, 2014. Hydrogen from biogas: catalytic tri-reforming process with Ni/La-Ce-O mixed oxides. *Appl. Catal. B Environ.* 148–149, 91–105.
- Piras, A., Colussi, S., Trovarelli, A., Sergo, V., Llorca, J., Psaro, R., Sordelli, L., 2005. Structural and morphological investigation of ceria-promoted Al₂O₃ under severe reducing/oxidizing conditions. *J. Phys. Chem. B* 109, 11110–11118.
- Plou, J., Durán, P., Herguido, J., Peña, J.A., 2014. Purified hydrogen from synthetic biogas by joint methane dry reforming and steam-iron process: behaviour of metallic oxides and coke formation. *Fuel* 118, 100–106.
- Pompeo, F., Nichio, N.N., Souza, M.M.V.M., Cesar, D.V., Ferretti, O.A., Schmal, M., 2007. Study of Ni and Pt catalysts supported on a-Al₂O₃ and ZrO₂ applied in methane reforming with CO₂. *Appl. Catal. A* General 316, 175–183.
- Rahemi, N., Haghghi, M., Babaloo, A.A., Fallah Jafari, M., Estifaei, P., 2013. Synthesis and physicochemical characterizations of Ni/Al₂O₃-ZrO₂ nanocatalyst prepared via impregnation method and treated with non THERMAL plasma for CO₂ reforming of CH₄. *J. Ind. Eng. Chem.* 19, 1566–1576.
- Rostrup-Nielsen, J.R., 1984. Sulfur-passivated nickel catalysts for carbon-free steam reforming of methane. *J. Catal.* 85, 31–43.
- Rostrup-Nielsen, J.R., 1995. Innovation and the catalytic process industry—the science and the challenge. *Chem. Eng. Sci.* 50, 4061–4071.
- Rostrup-Nielsen, J.R., Hansen, J.H.B., 1993. CO₂ reforming of methane over transition metals. *J. Catal.* 144, 38–49.
- Sajjadi, S.M., Haghghi, M., Alizadeh Eslami, A., Rahmani, F., 2013. Hydrogen production via CO₂-reforming of methane over Cu and Co doped Ni/Al₂O₃ nano-catalyst: impregnation vs. sol-gel method and effect of process conditions and promoter. *J. Sol Gel Sci. Technol.* 67, 601–617.
- Serrano-Lotina, A., Daza, L., 2014. Long-term stability test of Ni-based catalyst in carbon dioxide reforming of methane. *Appl. Catal. A* General 474, 107–113.
- Seung-hoon, K., Jae-sun, J., Eun-hyeok, Y., Kwan-Young, L., Ju, M.D., 2014. Hydrogen production by steam reforming of biomass-derived glycerol over Ni-based catalysts. *Catal. Today* 228, 145–151.
- Shyu, J.Z., Weber, W.H., Gandhi, H.S., 1988. Surface characterization of alumina-supported ceria. *J. Phys. Chem.* 92, 4964–4970.
- Slagtern, A., Schuurman, Y., Leclercq, C., Verykios, X., Mirodatos, C., 1997. Specific features concerning the mechanism of methane reforming by carbon dioxide over Ni/Al₂O₃ catalyst. *J. Catal.* 172, 118–126.
- Stagg-Williams, S.M., Noronha, F.B., Fendley, G., Resasco, D.E., 2002. CO₂ reforming of CH₄ over Pt/ZrO₂. Catalysts promoted with La and Ce oxides. *J. Catal.* 194, 240–249.
- Stewart, W.E., Caracotsios, M., Sorenson, J.P., 1992. Parameter estimation from multiresponse data. *AIChE J.* 38, 641–650.
- Sutthiumporn, K., Kawi, S., 2011. Promotional effect of alkaline earth over Ni-La₂O₃ catalyst for CO₂ reforming of CH₄: role of surface oxygen species on H₂ production and carbon suppression. *Int. J. Hydrogen Energy* 36, 14435–14446.
- Taylor, K.C., 1993. Nitric oxide catalysis in automotive exhaust systems. *Catal. Rev. Sci. Eng.* 35, 457–481.
- Therdthianwong, S., Siangchin, C., Therdthianwong, A., 2008. Improvement of coke resistance of Ni/Al₂O₃ catalyst in CH₄/CO₂ reforming by ZrO₂ addition. *Fuel Process. Technol.* 89, 160–168.
- Thyssen, V.V., Maia, T.A., Assaf, E.M., 2013. Ni supported on La₂O₃-SiO₂ used to catalyze glycerol steam reforming. *Fuel* 105, 358–363.
- Trovarelli, A., 1996. Catalytic properties of ceria and CeO₂-containing materials. *Catal. Rev. Sci. Eng.* 38, 439–520.
- Tsakiroglou, C.D., Theodoropoulou, M.A., Karoutsos, V., 2003. Nonequilibrium capillary pressure and relative permeability curves of porous media. *AIChE J.* 49, 2472–2486.
- Tzounis, L., Kirsten, M., Simon, F., Mäder, E., Stamm, M., 2014. The interphase microstructure and electrical properties of glass fibers covalently and non-covalently bonded with multiwall carbon nanotubes. *Carbon* 73, 310–324.
- Tzounis, L., Gärtner, T., Liebscher, M., Pötschke, P., Stamm, M., Voit, B., Heinrich, G., 2014. Influence of cyclic butylene terephthalate oligomer on processability and thermoelectric properties of polycarbonate/MWCNT nanocomposites. *Polymer* 55, 5381–5388.
- Tzounis, L., Debnath, S., Rooj, S., Fischer, D., Mäder, E., Das, A., Stamm, M., Heinrich, G., 2014. High performance natural rubber composites with a hierarchical reinforcement structure of carbon nanotube modified natural fibers. *Mater. Des.* 58, 1–11.
- Udengaard, N.R., Bak Hansen, J.H., Hanson, D.C., Stal, J.A., 1992. *Oil Gas J.* 90, 62.
- Verykios, X.E., 2003. Catalytic dry reforming of natural gas for the production of chemicals and hydrogen. *Int. J. Hydrogen Energy* 28, 1045–1063.
- Verykios, X.E., Mac Donald, S.M., Affrossman, S., 1996. Comparative study of carbon dioxide reforming of methane to synthesis gas over Ni/Al₂O₃ and conventional nickel-based catalysts. *J. Phys. Chem.* 100, 744–754.
- Wagner, R.S., Ellis, W.C., 1964. Vapor – liquid – solid mechanism of single crystal growth. *Appl. Phys. Lett.* 4, 89–90.
- Wang, S.B., Lu, G.Q.M., 1998. Role of CeO₂ in Ni/CeO₂-Al₂O₃ catalysts for carbon dioxide reforming of methane. *Appl. Catal. B Environ.* 19, 267–277.
- Wode, F., Tzounis, L., Kirsten, M., Constantinou, M., Georgopoulos, P., Rangou, S., Zafeiropoulos, N.E., Avgeropoulos, A., Stamm, M., 2012. Selective localization of multi-wall carbon nanotubes in homopolymer blends and a diblock copolymer. Rheological orientation studies of the final nanocomposites. *Polymer* 53, 4438–4447.
- Xiangyu, L., Chen, J.-F., Tan, Y., Zhang, Y., 2012. A highly dispersed nickel supported catalyst for dry reforming of methane. *Catal. Commun.* 20 (6), 6–11.
- Xu, J., Froment, G.F., 1989. Methane steam reforming, methanation and water–gas shift: I. Intrinsic kinetics. *AIChE J.* 35, 88–96.
- Xue, Q.S., Gao, L.D., Lu, Y., 2009. Sulfur-tolerant Pt/Gd₂O₃-CeO₂-Al₂O₃ catalyst for high efficiency H₂ production from autothermal reforming of retail gasoline. *Catal. Today* 146, 103–109.
- Yang, R., Xing, C., Lv, C., Shi, L., Tsubaki, N., 2010. Promotional effect of La₂O₃ and CeO₂ on Ni/γ-Al₂O₃ catalysts for CO₂ reforming of CH₄. *Appl. Catal. A* General 385, 92–100.
- Zhai, X., Ding, S., Liu, Z., Jin, Y., Cheng, Y., 2011. Catalytic performance of Ni catalysts for steam reforming of methane at high space velocity. *Int. J. Hydrogen Energy* 36, 482–489.
- Zhang, Z., Verykios, X.E., Mac Donald, S.M., Affrossman, S., 1996. Comparative study of carbon dioxide reforming of methane to synthesis gas over Ni/Al₂O₃ and conventional nickel-based catalysts. *J. Phys. Chem. C* 100, 744–754.